

AD-A185 130

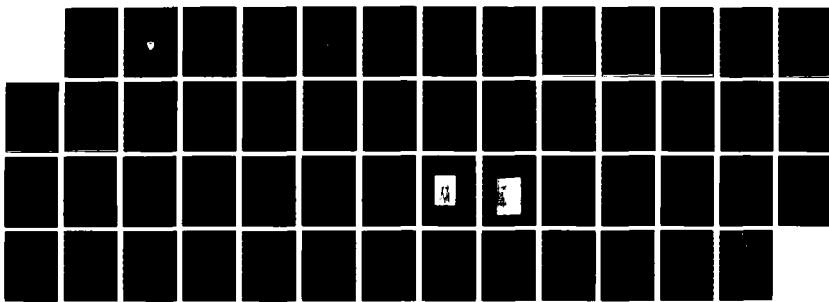
FINAL REPORT ON CONTRACT F49620-85-C-0026 VOLUME 2(U)
PRINCETON UNIV NJ DEPT OF MECHANICAL AND AEROSPACE
ENGINEERING S A OR52AQ MAY 87 AFOSR-TR-87-1349-VOL-2
F49620-85-C-0026

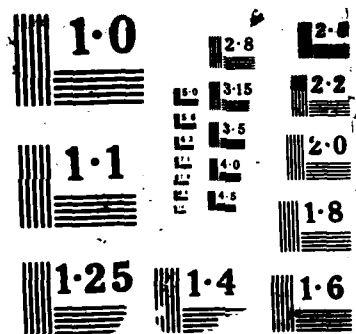
1/1

UNCLASSIFIED

F/0 26/4

ML





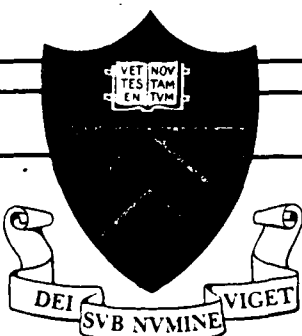
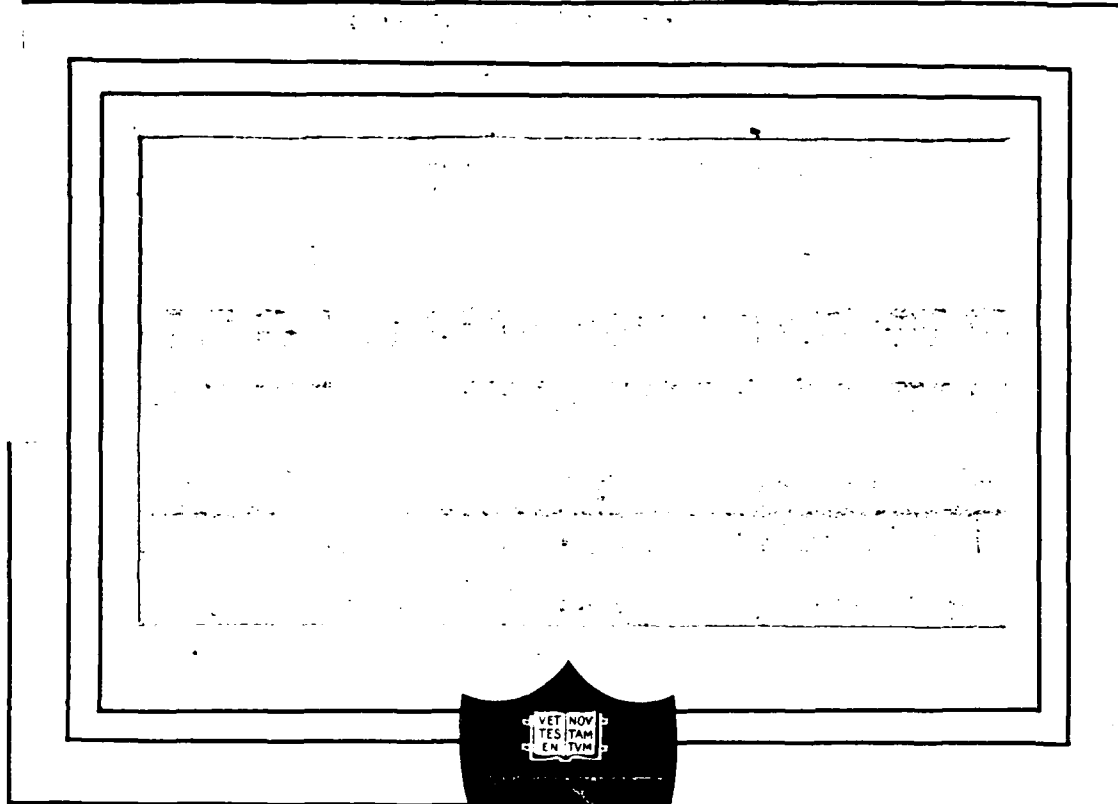
AD-A185 130

DTIC FILE COPY

(2)

AFOSR, TM:

87-1349



DTIC
SELECTED
SEP 30 1987
S D
& D

DISTRIBUTION STATEMENT A
Approved for public release
Distribution Unlimited

PRINCETON UNIVERSITY

87 9 24 250

AD A125-136

REPORT DOCUMENTATION PAGE

1a. REPORT SECURITY CLASSIFICATION Unclassified		1b. RESTRICTIVE MARKINGS	
2a. SECURITY CLASSIFICATION AUTHORITY		3. DISTRIBUTION/AVAILABILITY OF REPORT Approved for Public Release; distribution is unlimited	
3b. DECLASSIFICATION/DOWNGRADING SCHEDULE		5. MONITORING ORGANIZATION REPORT NUMBER(S) AFOSR-TR-87-1340	
4. PERFORMING ORGANIZATION REPORT NUMBER(S)	6a. NAME OF PERFORMING ORGANIZATION Princeton University		
6b. OFFICE SYMBOL (If applicable)	7a. NAME OF MONITORING ORGANIZATION AFOSR/NA		
6c. ADDRESS (City, State and ZIP Code) Princeton University Princeton, NJ 08544	7b. ADDRESS (City, State and ZIP Code) Building 410 Bolling AFB DC 20332-6448		
8a. NAME OF FUNDING/SPONSORING ORGANIZATION AFOSR/NA	8b. OFFICE SYMBOL (If applicable)	9. PROCUREMENT INSTRUMENT IDENTIFICATION NUMBER F49620-85-C-0026	
9c. ADDRESS (City, State and ZIP Code) Bolling Air Force Base Washington, DC 20332-6448	Bldg 410	10. SOURCE OF FUNDING NOS.	
11. TITLE (Include Security Classification) Final Report on Contract F49620-85-C-0026 Vol. 2	12. PERSONAL AUTHORISI - Steven A. Orszag	PROGRAM ELEMENT NO. 61102F	PROJECT NO. 2307
13. TYPE OF REPORT Final Report	13b. TIME COVERED FROM 10/1/84 TO 11/30/86	14. DATE OF REPORT (Year, Month, Day) May, 1987	15. PAGE COUNT
16. SUPPLEMENTARY NOTATION			
COSATI CODES FIELD GROUP SUB. GR.		18. SUBJECT TERMS (Continue on reverse if necessary and identify by block numbers) Turbulence, Numerical Simulation	
19. ABSTRACT (Continue on reverse if necessary and identify by block numbers) This report consists of papers that summarize work done on this research project. The major results include: 1) The development and application of the renormalization group method to the calculation of fundamental constants of turbulence, the construction of turbulence transport models, and large-eddy simulations; 2) The application of RNG methods to turbulent heat transfer through the entire range of experimentally accessible Reynolds numbers; 3) The discovery that high Reynolds number turbulent flows tend to act as if they had weak nonlinearities, at least when viewed in terms of suitable 'quasi-particles'; 4) The further analysis of secondary instability mechanisms in free shear flows, including the role of these instabilities in chaotic, 3-D free shear flows; 5) The further development of numerical simulations of turbulent spots in wall bounded shear flows; 6) The study of cellular automata for the solution of fluid mechanical problems; 7) The clarification of the relationship between the hyperscale instability of anisotropic small-scale flow structures to long-wavelength perturbations and the cellular automaton description			
DISTRIBUTION/AVAILABILITY OF ABSTRACT CLASSIFIED/UNLIMITED <input checked="" type="checkbox"/> SAME AS RPT <input checked="" type="checkbox"/> DTIC USES <input type="checkbox"/>		21. ABSTRACT SECURITY CLASSIFICATION Unclassified	
NAME OF RESPONSIBLE INDIVIDUAL Dr James M McMichael		22b. TELEPHONE NUMBER (Include Area Code) (202) 767-4936	22c. OFFICE SYMBOL AFOSR/NA

STRACT, continued from other side

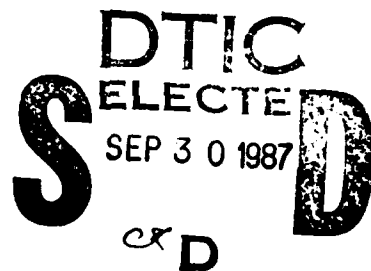
fluids; 8) The development of efficient methods to analyze the structure of strange attractors in the description of dynamical systems; 9) The analysis of interscale instability as a mechanism for destabilization of coherent flow structures.

(2)

**FINAL REPORT ON
AFOSR CONTRACT F49620-85-C-0026**

Steven A. Orszag, Principal Investigator
Department of Mechanical and Aerospace Engineering
Princeton University
Princeton, NJ 08544

Volume 2



DISTRIBUTION STATEMENT (A)
Approved for public release; Distribution Unlimited

Renormalization-Group Analysis of Turbulence

Victor Yakhot and Steven A. Orszag

Applied and Computational Mathematics, Princeton University, Princeton, New Jersey 08544
(Received 7 July 1986)

Using renormalization-group methods and the postulated equivalence between the *inertial-range structures* of turbulent flows satisfying initial and boundary conditions and of flows driven by a random force, we evaluate the Kolmogorov constant (1.617) and Batchelor constant (1.161), skewness factor (0.4878), power-law exponent (1.3307) for the decay of homogeneous turbulence, turbulent Prandtl number (0.7179), and von Kármán constant (0.372). This renormalization-group technique has also been used to derive turbulent transport models.

PACS numbers: 47.25.-c

The direct interaction approximation (DIA), due to Kraichnan,¹ was the first field-theoretical approach to the theory of turbulence. Formulated in terms of the Dyson equation, the DIA is characterized as the lowest-order approximation which includes nonlinear corrections to the propagator for the mode $v(\mathbf{k}, \omega)$. It was shown¹ that, in the inertial range, the DIA gives the energy spectrum $E(k) \propto k^{-5/2}$. This result contradicts both experimental data and the Kolmogorov theory of turbulence which gives $E(k) \propto k^{-5/3}$, perhaps with small corrections due to intermittency.

The source of this discrepancy between the DIA and the Kolmogorov theory has long been understood.² The DIA does not distinguish between dynamic and kinematic interactions between eddies of widely separated length scales. Small eddies are convected by large eddies in a purely kinematic way which should not lead to energy redistribution between scales. The spurious effect of large-scale convection on small scales has been removed from the DIA by use of a Lagrangean description of the flow. This Lagrangean-

history direct interaction approximation³ (LHDIA) leads to the Kolmogorov 5/3-energy spectrum with the Kolmogorov constant $C_K = 1.77$ [see (11) below] which is in reasonable agreement with experiment.⁴ However, application of the LHDIA to the problem of turbulent diffusion of a passive scalar does not lead to quantitative agreement with experimental data: The turbulent Prandtl number P_t , calculated⁴ from the LHDIA is roughly 0.14, much smaller than the experimentally observed $P_t = 0.7-0.9$.

In 1977 Forster, Nelson, and Stephen⁵ used dynamic renormalization-group (RG) methods, originally developed for the description of the dynamics of critical phenomena,⁶ to derive velocity correlations generated by the Navier-Stokes equation with a random-force term. The ideas expressed in Ref. 5 have been used by others in the context of hydrodynamic turbulence.⁷⁻¹⁰ The problem is formulated as follows: Consider the d -dimensional space-time Fourier-transformed Navier-Stokes equation for incompressible flow,

$$v_i(\hat{\mathbf{k}}) = G^0 f_i(\hat{\mathbf{k}}) - \frac{1}{2} i \lambda_0 G^0 P_{lmn}(\mathbf{k}) \int v_m(\hat{\mathbf{q}}) v_n(\hat{\mathbf{k}} - \hat{\mathbf{q}}) d^d q / (2\pi)^{d+1}, \quad (1)$$

where the zero-mean Gaussian random force $f(\mathbf{k}, \omega)$ is determined by its correlation function

$$\langle f_i(\mathbf{k}, \omega) f_j(\mathbf{k}', \omega') \rangle = (2\pi)^{d+1} 2 D_0 k^{-y} P_{ij}(\mathbf{k}) \delta(\hat{\mathbf{k}} - \hat{\mathbf{k}}'). \quad (2)$$

Here

$$G^0 = (-i\omega + \nu_0 k^2)^{-1}, \quad P_{ij}(\mathbf{k}) = \delta_{ij} - k_i k_j / k^2, \quad P_{ijk}(\mathbf{k}) = k_i P_{jk}(\mathbf{k}) + k_j P_{ik}(\mathbf{k}). \quad (3)$$

$\hat{\mathbf{k}} = (\mathbf{k}, \omega)$, ν_0 is the kinematic viscosity, $\lambda_0 = 1$, and the constant $y > -2$. The problem (1)-(3) is formulated on the interval $0 < k \leq \Lambda_0$ and $-\infty < \omega < \infty$, where Λ_0 is a wave number beyond the dissipation wave number at which substantial modal excitations cease. The parameter D_0 , which determines the intensity of the random force, is discussed below.

The RG procedure consists of the elimination of modes $v^>(\mathbf{k})$ with wave vectors satisfying $\Lambda_0 e^{-y}$

$< k < \Lambda$ from the equations of motion for the modes $v^<(\mathbf{k})$ with wave vectors from the interval $0 < k < \Lambda_0 e^{-y}$. At this stage, kinematic interactions are excluded by construction and one can expect physically meaningful results in the limit $k \rightarrow 0$. Details of this RG procedure are given elsewhere.^{5,11}

The RG scale-elimination procedure gives a correction to the bare viscosity ν_0 in terms of an effective viscosity which takes into account the effect of the



eliminated modes. The result is

$$v_r = v_0 [1 + A_d \bar{\lambda}_0^2 (\epsilon^{dr} - 1)/\epsilon], \quad (4)$$

where $\epsilon = 4 - y - d$, $A_d = \tilde{A}_d S_d / (2\pi)^d$, and

$$\tilde{A}_d = \frac{1}{2} \frac{d^2 - d - \epsilon}{d(d-2)}, \quad S_d = \frac{(2\pi)^{d/2}}{\Gamma(\frac{1}{2}d)}. \quad (5)$$

The dimensionless expansion parameter $\bar{\lambda}_0$ (which is a Reynolds number) is defined as $\bar{\lambda}_0 = D_0/v_0 \Lambda_0^2$. As we shall see below, the choice of $y = d$ recovers the Kolmogorov scaling in the inertial range.

By variation of the cutoff $\Lambda(r) = \Lambda_0 e^{-r}$ we derive differential-recursion relations for $\bar{\lambda}(r) = [D_0/v(r)] \times \Lambda(r)^{3/2}$ and $v(r)$ ¹¹:

$$\frac{dv}{dr} = A_d v(r) \bar{\lambda}^2(r), \quad \frac{d\bar{\lambda}^2}{dr} = \bar{\lambda}^2 (\epsilon - 3 A_d \bar{\lambda}^2). \quad (6)$$

The solutions to (6) are

$$\bar{\lambda}(r) = \bar{\lambda}_0 e^{\epsilon r/2} [1 + 3 A_d \bar{\lambda}_0^2 (\epsilon^{dr} - 1)/\epsilon]^{-1/2},$$

$$v(r) = v_0 [1 + 3 A_d \bar{\lambda}_0^2 (\epsilon^{dr} - 1)/\epsilon]^{1/2}.$$

In the limit $r \rightarrow \infty$ the coupling parameter $\bar{\lambda}$ (which is an effective Reynolds number) goes to the fixed point

$$\bar{\lambda}_* = (\epsilon/3 A_d)^{1/2}$$

and

$$v(\Lambda) = (\frac{1}{4} A_d D_0)^{1/3} \Lambda^{-4/3}.$$

Eliminating all modes with $q > k$, we set $\Lambda = k$ and obtain

$$v(k) = (\frac{1}{4} A_d D_0)^{1/3} k^{-4/3} \quad (7)$$

$$= 0.4217 [2 D_0 S_d / (2\pi)^d]^{1/3} k^{-4/3}$$

when $y = d = 3$. The coefficient \tilde{A}_d is computed from (5) in the lowest order of ϵ expansion ($\epsilon = 0$); thus $\tilde{A}_d = 0.2$ in the three-dimensional case $d = 3$.

The energy spectrum can be calculated to lowest order in ϵ from the equation $v(k) = G(k)f(k)$, where the propagator $G(k)$ is evaluated with the k -dependent viscosity (7). The result is

$$E(k) = 1.186 [2 D_0 S_d / (2\pi)^d]^{1/3} k^{-5/3}. \quad (8)$$

Thus the renormalization-group procedure applied to randomly stirred fluid gives the Kolmogorov spectrum in the case $y = d$.

In order to complete the analysis, it is necessary to relate the parameter D_0 to observables. Consider a fluid described by the Navier-Stokes equation

$$\frac{\partial \mathbf{v}}{\partial t} + (\mathbf{v} \cdot \nabla) \mathbf{v} = -\frac{1}{\rho} \nabla p + v_0 \nabla^2 \mathbf{v}, \quad (9)$$

subject to initial and boundary conditions. We assume that strongly turbulent fluid is characterized in the

inertial range of scales by statistically universal scaling laws (Kolmogorov spectrum, etc.) which are independent of initial and boundary conditions. Thus, the system in the universal regime can be described by equations of motion which do not involve any particular initial and boundary conditions: (1) and (2), for example, provided that the random force in (1) and (2) is chosen in such a way that it generates velocity fluctuations which are statistically equivalent to the solutions of (9) subject to initial and boundary conditions. In other words, to describe the fluid in the inertial range we may replace (9) with the corresponding system (1), (2) with a properly chosen force. In this case, it has been shown¹² that if we assume that solutions of Eq. (9) in the inertial range scale as

$$v(k) = N \mathcal{E}^{1/3} k^{-4/3} \quad (10)$$

and

$$E(k) = C_K \mathcal{E}^{2/3} k^{-5/3}, \quad (11)$$

then energy balance in analytical turbulence theory requires that the Kolmogorov constant C_K in (11) and the parameter N in (10) be related as

$$N/C_K^2 = 0.1904.$$

Here \mathcal{E} is the rate of energy dissipation in the fluid. Demanding the equivalence of (7) and (8) with (10) and (11) in the inertial range gives

$$2 D_0 S_d / (2\pi)^d = 1.594 \mathcal{E}, \quad (12)$$

so that $C_K = 1.617$.

A similar RG procedure¹¹ applied to the equation of a passive scalar gives the result that the turbulent Prandtl number P_t in the case $y = d = 3$ is

$$P_t^{-1} = \frac{1}{2} \left[-1 + \left(1 + \frac{4(d-1)}{d} \tilde{A}_3^{-1} \right)^{1/2} \right] = 1.3929,$$

so that $P_t = 0.7179$. The Batchelor constant C_{Ba} is defined by the inertial-range scalar fluctuation spectrum. Using energy balance in terms of the k -dependent viscosity at the fixed point, we find¹¹ $C_{Ba} = C_K P_t$, so that $C_{Ba} = 1.161$. Another calculation¹³ of C_{Ba} , based on an RG-modified version of the direct-interaction approximation, gives the same result. The results for the turbulent Prandtl number and the Batchelor constant are in close agreement with experimental data.¹⁴

The renormalization-group procedure can also be used for deriving averages of different nonlinear operators over the fluctuating velocity field.¹¹ For example, the skewness factor, which is a dimensionless measure of nonlinear transfer, is defined as

$$g = -\frac{\langle (\partial v_i / \partial x_1)^3 \rangle}{\langle (\partial v_i / \partial x_1)^2 \rangle^{3/2}} = \frac{A}{B^{1/2}}, \quad (13)$$

where $\langle \dots \rangle$ denotes average over the fluctuating velocity field, and

$$A = \langle (\partial v_1 / \partial x_1)^3 \rangle = -i \int q_1 p_1 (k - q - p) v_1(q) v_1(p) v_1(k - q - p) d^d q d^d p / (2\pi)^{d+2}$$

in the limit $k \rightarrow 0$. Decomposing the velocity field into the components $v^<$ and $v^>$ and eliminating small scales using the forced Navier-Stokes equation (1), (2), we find, in the lowest order in the ϵ expansion, that¹¹

$$\begin{aligned} A^< &= -i \int q_1 p_1 (k - q - p) v_1^<(q) v_1^<(p) v_1^<(k - q - p) d^d q d^d p / (2\pi)^{d+2} \\ &= -\frac{1}{420} [2D_0 S_d / (2\pi)^d] \delta / \nu^3 \Lambda^2 \end{aligned}$$

in the limit $k \rightarrow 0$ ($r \rightarrow \infty$). The same procedure applied to evaluation of B in (13) gives

$$B^< = \frac{1}{20} \frac{2D_0 S_d / (2\pi)^d}{\nu}$$

in the limit $k \rightarrow 0$ ($r \rightarrow \infty$). Thus

$$S^<(r) = -\frac{A^<}{(B^<)^{3/2}} = 0.1336 \left\{ \frac{2D_0 S_d / (2\pi)^d}{\nu^3 \Lambda^4} \right\}^{1/2} = 0.4878 \quad (14)$$

when calculated at the fixed point of the RG calculation. Since $S^<(r)$ does not depend on r in the limit $r \rightarrow \infty$, we assume that (14) holds everywhere in the inertial range, and so $S = 0.4878$. It should also be noted that the same RG procedure gives the exact result $S = 0$ in the two-dimensional case $d = 2$.

Another important relation can be derived from the Kolmogorov energy spectrum and formula (7) for the turbulent viscosity. It can be checked readily that the total kinetic energy K in the system is $K = 1.195 \delta / \nu \Lambda^2$, where Λ is the wave vector corresponding to the integral scale of turbulence. Combining this relation with (7) and (12) we derive a relation between ν , kinetic energy K , and the mean dissipation rate δ , namely, $\nu = 0.0837 K^2 / \delta$.

The RG procedure can be used to evaluate each term of the equations of motion for kinetic energy and dissipation rate. This leads to a so called K - δ model of turbulence. It can be shown¹¹ that this RG model implies that isotropic turbulence decays as $K \propto (t - t_0)^{-1.3307}$ which is close to the experimental data¹⁴ and recent results of direct numerical simulations.¹⁵ The same model, which does not involve any experimentally adjustable parameters, gives the von Kármán constant¹¹ $\kappa = 0.372$ for the logarithmic velocity profile.

The good agreement of the RG-predicted constants (C_K , C_B , P , S , κ) with experimental data is to some extent surprising since the RG procedure does not take into account local interactions between eddies of similar size. However, it has been pointed out⁹ that the ratio of time constants which correspond to nonlocal and local interactions is $O(\epsilon^{1/2})$. Thus, local interactions are weak if ϵ is assumed small. It remains to be explained why the lowest-order truncation of the

RG expansion in powers of $\epsilon = 4$ works so well.

- ¹R. H. Kraichnan, J. Fluid Mech. 5, 497 (1959).
- ²R. H. Kraichnan, Phys. Fluids 7, 1723 (1964).
- ³R. H. Kraichnan, Phys. Fluids 8, 575 (1965).
- ⁴R. H. Kraichnan, Phys. Fluids 9, 1728 (1966).
- ⁵D. Forster, D. Nelson, and M. Stephen, Phys. Rev. A 16, 732 (1977).
- ⁶S. K. Ma and G. Mazenko, Phys. Rev. 11, 4077 (1975).
- ⁷C. De Dominicis and P. C. Martin, Phys. Rev. A 19, 419 (1979).
- ⁸J. D. Fournier and U. Frisch, Phys. Rev. A 17, 747 (1978).
- ⁹J. D. Fournier and U. Frisch, Phys. Rev. A 28, 1000 (1983).
- ¹⁰V. Yakhot, Phys. Rev. A 23, 1486 (1981).
- ¹¹V. Yakhot and S. A. Orszag, J. Sci. Comput. 1, 1 (1986).
- ¹²R. H. Kraichnan, J. Fluid Mech. 47, 525 (1971).
- ¹³W. Dannevik and V. Yakhot, to be published.
- ¹⁴A. S. Monin and A. M. Yaglom, in *Statistical Fluid Mechanics*, edited by John Lumley (MIT Press, Cambridge, 1975), Vol. 2.
- ¹⁵M. J. Lee and W. C. Reynolds, Stanford University Report No. TF-24, 1985 (unpublished).

Heat transfer in turbulent fluids—I. Pipe flow

VICTOR YAKHOT, STEVEN A. ORSZAG and ALEXANDER YAKHOT[†]

Applied and Computational Mathematics, Princeton University, Princeton, NJ 08544, U.S.A.

(Received 21 October 1985 and in final form 24 March 1986)

Abstract —The expression for turbulent Prandtl number obtained from the renormalization group procedure is used to describe the process of heat transfer in turbulent pipe flow. The results are in a good agreement with experimental data over the entire range of experimentally accessible Prandtl numbers, $10^{-2} < \sigma_0 < 10^0$.

1. INTRODUCTION

THE PROBLEM of heat conduction in turbulent flows has been under intensive study for more than half a century. Experimental data on velocity and temperature distributions have suggested many semi-empirical theories to describe the basic properties of the phenomenon.

It has long been realised that, if the Reynolds number is large enough and the Prandtl number $\sigma_0 = v_0/\kappa_0$ is not too small, the molecular diffusivity κ_0 does not play any role in the process of heat conduction or diffusion in turbulence. In this case, the temperature and velocity distributions have similar behavior in the wall region, both obeying the logarithmic law with the temperature profile

$$\langle T \rangle = \sigma_{\text{turb}} \frac{q}{bpc_p u_*} (\ln y + C).$$

Here $\langle \rangle$ denotes a horizontal average, y is the distance to the wall, q denotes the constant heat flux and c_p and u_* are the heat capacity and friction velocity, respectively. The Von Karman constant $b \approx 0.4$ and $\sigma_{\text{turb}} = v_{\text{turb}}/\kappa_{\text{turb}}$ is the ratio of turbulent viscosity to turbulent heat conductivity. According to the well-known Prandtl-Reynolds-Colburn analogy, the turbulent Prandtl number is nearly a universal constant: $\sigma_{\text{turb}} = 0.7-0.9$.

In the limiting case of small Prandtl number, the molecular diffusivity κ_0 cannot be neglected and the simple analogy between temperature and velocity distributions does not work. It is clear, however, that as $\sigma_0 \rightarrow 0$, the Nusselt number Nu [defined below as the dimensionless (based on the bulk temperature, see equation (28)) heat flux] satisfies $Nu \approx \text{const}$. It is known from experiments that $Nu \approx 6.8-7.0$ in flows with constant heat flux through the wall while Nu is somewhat smaller in flows with constant wall temperature. To the best of our knowledge, there is no satisfactory theory describing heat conductivity in turbulent flow with low Prandtl number.

Many attempts have been made to find empirical

and semi-empirical relations to describe turbulent heat transfer across a wide range of Prandtl and Reynolds numbers. More than 30 formulae of this kind have been reviewed by Reynolds [1] in 1975. In 1979, Gori *et al.* [2] concluded that there is no general way to describe turbulent heat transfer in low-Prandtl-number fluids for a wide range of Re . They suggested the following formula for the turbulent Prandtl number σ_{turb} when $Re < 1.7 \times 10^5$:

$$\sigma_{\text{turb}}^{-1} = 0.014 Re^{0.45} \sigma_0^{0.2} \times \{1 - \exp[-(0.014 Re^{0.45} \sigma_0^{0.2})^{-1}]\} \quad (1)$$

as proposed by Aoki [3] or

$$\sigma_{\text{turb}}^{-1} = (1 + 100 Pe^{-0.5})[(1 + 120 Re^{-0.5})^{-1} - 0.15] \quad (2)$$

as proposed by Reynolds [1]. The formula

$$\sigma_{\text{turb}} = 0.85 + 0.005 \sigma_0^{-1} \quad (3)$$

proposed by Jischa and Rieke [4], was suggested to represent the Reynolds number range $1.7 \times 10^5 < Re < 2.6 \times 10^5$; the constant $\sigma_{\text{turb}} = 0.85$ was used for $Re > 2.6 \times 10^5$. When relations (1)-(3) are used to predict the mean temperature field, they give reasonably accurate predictions of the Nusselt number (which is related to the wall gradient of the temperature profile). However, the full temperature profiles predicted on the basis of expressions (1)-(3) were less satisfactory.

In this work we apply a formula for the turbulent Prandtl number derived by Yakhot and Orszag [5] to describe heat transfer in pipe flows. It will be shown in Section 3 that the proposed relation between turbulent viscosity and turbulent heat conductivity gives accurate predictions of both Nusselt number and temperature distributions across an extremely wide range of Prandtl and Nusselt numbers.

2. FORMULAE FOR TURBULENT PRANDTL NUMBER

Here we present some of the basic ideas leading to an expression for the turbulent Prandtl number. The main steps of the renormalization group procedure are

[†] Department of Mechanical Engineering, University of Ben Gurion of the Negev, Beer-Sheva 84105, Israel

NOMENCLATURE

<i>A</i>	Van Driest parameter	<i>q</i>	heat flux
<i>B</i>	proportionality coefficient in x-coordinate dependence of temperature, equation (20)	<i>r</i> _*	wall coordinate, ru_*/v_0
<i>A_d</i>	geometric factor, equation (11)	<i>u</i>	mean velocity in x-direction
<i>C</i>	constant in the temperature profile, equation (30)	<i>u_*</i>	friction velocity
<i>C_h</i>	heat transfer coefficient	<i>u₊</i>	dimensionless velocity, u/u_*
<i>D</i>	pipe diameter	<i>v_i</i>	components of velocity.
<i>G⁰</i>	bare propagator for velocity		
<i>Nu</i>	Nusselt number (based on the bulk temperature), $C_h \sigma_0 Re$		
<i>Pe</i>	Péclet number, $\sigma_0 Re$		
<i>R</i>	radius of pipe		
<i>Re</i>	Reynolds number based on the pipe diameter, $u_*/D/v_0$		
<i>R_*</i>	Reynolds number based on the friction velocity, $u_*/R/v_0$		
<i>T</i>	temperature		
<i>T_c</i>	temperature at the center		
<i>T_w</i>	temperature at the wall		
<i>T_*</i>	characteristic temperature, $q/c_p \rho u_*$		
<i>T₊</i>	dimensionless temperature, T/T_*		
<i>a, b</i>	parameters in equations (12)-(14)		
<i>c_p</i>	heat capacity		
<i>d</i>	fixed-point parameter [5], 7 in this work		
<i>g⁰</i>	bare propagator for temperature		

			where f is the velocity spectrum scales).
			It has been random function:
			$\langle f(k, \alpha) f \rangle$
			with P the velocity mogorov's dissipation of the fluid scales, to the
			This fact for elimination either turb renormaliz for an infinit [6]. Martin these works characteriz

			In such sys determined with bound basic ideas of given in the
			It has been the Navier-St field ψ in w removed is

outlined in the Appendix. The details of the calculations are given elsewhere [5]. In this paper, we are interested in application of the final result to the problem of heat transfer in turbulent flow in a pipe. This will be done in the next section.

The most distinguishing characteristic of a turbulent flow is approximate universality of the properties of scales much smaller than any integral scale L in the flow. The high Reynolds number turbulent flow is characterized by three different ranges of spatial scales. (1) For wave-numbers $k > \pi/L$ the energy spectrum is strongly anisotropic and is not characterized in any universal way. The integral scale reflects both geometry of the flow and the physico-chemical processes taking place there. (2) At much smaller scales, with wave-numbers satisfying $\pi L \ll k < k_d = Re^{1/4}L^{-1}$, the velocity fluctuation spectrum is approximately given by the Kolmogorov energy spectrum $E(k) = C_k k^{2/3} L^{-5/3}$, with the Kolmogorov constant $C_k = 1.3-2.3$. (3) In the dissipation range ($k > k_d$) the energy spectrum decreases exponentially with k .

Universality of the small scales can be formulated in the language of theoretical hydrodynamics: the fluid

described by the Navier-Stokes equation

$$\frac{\partial v_i}{\partial t} + v_j \frac{\partial v_i}{\partial x_j} = - \frac{\partial p}{\partial x_i} + v_0 \frac{\partial^2 v_i}{\partial x_j \partial x_j} \quad (4)$$

$$\frac{\partial v_i}{\partial x_i} = 0$$

subject to initial and boundary conditions, is characterized at the small scales by the 5/3-Kolmogorov spectrum. This property does not depend on boundary conditions which are usually characterized at large scales. Boundary conditions can be considered from the viewpoint of small scales as a source of energy injected into the large scales which subsequently cascade to the small scales. Using the analogy with equilibrium statistical mechanics in which the results are independent of the details of the interaction of the system with a heat bath, we replace (4) by the more general equation (5) and add the heat transfer equation (6).

$$\frac{\partial v_i}{\partial t} + v_j \frac{\partial v_i}{\partial x_j} = f_i - \frac{\partial p}{\partial x_i} + v_0 \frac{\partial^2 v_i}{\partial x_j \partial x_j} \quad (5)$$

$$\frac{\partial v_i}{\partial x_i} = 0$$

Here the total
molecular and
the following

where the $H(x)$ is the
of turbulence
[2d(1+2d)]
been shown
elimination
of a passive
between the eq
the total visc

$$\frac{\partial T}{\partial t} + \bar{v}_i \frac{\partial T}{\partial x_i} = \kappa_0 \frac{\partial^2 T}{\partial x_i \partial x_i} \quad (6)$$

where \mathbf{f} is the random force (noise) chosen to generate the velocity field \mathbf{v} described by the Kolmogorov spectrum in the limit of large wave-vectors (small scales).

It has been shown by Yakhut [8] that the Gaussian random force \mathbf{f} characterized by the correlation function:

$$\langle f_i(k, \omega) f_j(k', \omega') \rangle \approx \bar{\epsilon} k^{-3} P_{ij}(k) \delta(k+k') \delta(\omega+\omega') \quad (7)$$

with $P_{ij}(k) = \delta_{ij} - k_i k_j / k^2$, generates small-scale velocity fluctuations characterized by the Kolmogorov spectrum. The parameter $\bar{\epsilon}$ in (7) denotes the dissipation rate of the turbulent energy per unit mass of the fluid and relates the force \mathbf{f} , acting on small scales, to the energy input taking place at large scales.

This fact is the basis for using the random force (7) for elimination of small scales in the construction of either turbulent sub-grid or transport models. The renormalization-group method (RNG) was developed for an infinite, homogeneous medium by Forster *et al.* [6], Martin and DeDominics [7] and Yakhut [8]. In these works, $\bar{\epsilon}$ has been treated as a given parameter characterizing the rate of stirring. In finite systems

$$\bar{\epsilon} = \frac{1}{T} \frac{1}{V} \int dt \int \epsilon(x, t) dx \quad (8)$$

$$\epsilon(x, t) = \frac{v_0}{2} \left(\frac{\partial \bar{v}_i}{\partial x_j} + \frac{\partial \bar{v}_j}{\partial x_i} \right)^2. \quad (9)$$

In such systems, $\bar{\epsilon}$ is a quantity that should be determined dynamically from the equations of motion with boundary and initial conditions applied. The basic ideas of the renormalization group procedure are given in the Appendix.

It has been shown by Yakhut and Orszag [9] that the Navier-Stokes equations for the mean velocity field \bar{v}_i in which the fluctuating contributions are removed is:

$$\frac{\partial \bar{v}_i}{\partial t} + \bar{v}_j \frac{\partial \bar{v}_i}{\partial x_j} = - \frac{\partial p}{\partial x_i} + \frac{\bar{\epsilon}}{\Lambda_t} v \frac{\partial \bar{v}_i}{\partial x_j}. \quad (10)$$

Here the total viscosity v takes into account both molecular and turbulent contributions and is given by the following relation [9]:

$$v = v_0 \left[1 + H \left(\frac{3}{8} \frac{A_d \bar{\epsilon}}{\Lambda_t^4 v_0^3} - 100 \right) \right]^{1/3} \quad (11)$$

where the ramp function $H(x) = x$ if $x > 0$ and $H(x) = 0$ if $x < 0$ and Λ_t is the inverse integral scale of turbulence [9]. The parameter $A_d = (d^2 - d) / [2d(d+2)] = 0.333$ since $d = 7$ for this problem. It has been shown by Yakhut and Orszag [5] that elimination of small scales from the equations (4)-(6) of a passive scalar leads to the following relation between the inverse total Prandtl number $\alpha = v^{-1}$ and the total viscosity v :

$$\left(\frac{x-a}{x_0-a} \right) \left(\frac{x+b}{x_0+b} \right)^{-1} = \frac{v_0}{v} \quad (12)$$

where

$$\gamma = \frac{a+1}{a+b}$$

$$a = \left[-1 + \left(1 + 8 \frac{d+2}{d} \right)^{1/2} \right] / 2 \quad (13)$$

$$b = a+1.$$

For $d = 7$, relation (12) becomes

$$\left(\frac{x-1.1793}{x_0-1.1793} \right)^{0.65} \left(\frac{x+2.1793}{x_0+2.1793} \right)^{-0.35} = \frac{v_0}{v}. \quad (14)$$

The result (14) expresses the inverse total Prandtl number α as a function of total viscosity v and is the main result to be studied in this paper.

According to (11), the turbulent viscosity is itself a function of the distance from the wall since Λ_t must be associated with the distance to the wall. One sees that in the region of fully developed turbulence where $v_0, v \ll 1$, the total Prandtl number $\sigma = \alpha^{-1} = 0.8476$, which is in a good agreement with available experimental data $\sigma = 0.7-0.9$ (see Landau and Lifshitz [10] and Monin and Yaglom [11]). Close to the wall where $v \approx v_0$, one finds from (14) that $\sigma \approx v_0 \kappa_0$. Thus, the equation of motion for the mean temperature can be written as:

$$\frac{\partial T}{\partial t} + \bar{v}_i \frac{\partial T}{\partial x_i} = \frac{\bar{\epsilon}}{\kappa} \frac{\partial T}{\partial x_i} \quad (15)$$

where $\kappa = xv$ is determined from (14). The dynamics of diffusion of a passive scalar is governed by the set of equations (10), (11), (14), (15).

We emphasize that these results do not include any experimentally adjustable parameters.

3. HEAT CONDUCTIVITY IN PIPE FLOW

Here we apply the results presented in the previous section to describe the process of heat transfer in turbulent flow through a pipe of radius R . The problem can be formulated in terms of the stationary Navier-Stokes equation

$$\frac{1}{r} \frac{\partial}{\partial r} \left(r v \frac{\partial u}{\partial r} \right) = \frac{\partial p}{\partial x} \quad (16)$$

and the heat transfer equation

$$\frac{1}{r} \frac{\partial}{\partial r} \left(\kappa v \frac{\partial T}{\partial r} \right) = u \frac{\partial T}{\partial x} \quad (17)$$

where v and κ are total viscosity and diffusivity, respectively. The parameters v and κ include both molecular and turbulent contributions. The total Prandtl number $\sigma = v\kappa$ is determined from relation (14).

We introduce the friction velocity $u_* = (\tau_w / \rho)^{1/2}$, wall coordinate r_* , nondimensional velocity u_* , and

nondimensional total viscosity ν_* :

$$r_* = r \frac{u_*}{v_0}, \quad u_* = u/u_*, \quad \nu_* = v/v_0. \quad (18)$$

The equation of motion now has the nondimensional form:

$$\frac{1}{r_*} \frac{\partial}{\partial r_*} \left(r_* v_* \frac{\partial u_*}{\partial r_*} \right) = -\frac{2}{R_*} \quad (19)$$

where $R_* = u_* R / v_0$ is the Reynolds number based on the friction velocity.

We consider heat transfer in a pipe with constant heat flux through the wall. In this case it is convenient to introduce a new variable Θ defined as:

$$T(x, r) = \Theta(r) + Bx. \quad (20)$$

Substituting (20) into (17) yields an equation for $\Theta(r)$:

$$\frac{1}{r_*} \frac{\partial}{\partial r_*} \left(r_* \kappa \frac{\partial \Theta}{\partial r_*} \right) = u_* B. \quad (21)$$

The parameter B can be expressed in terms of the imposed constant heat flux. Integrating (21) over r and using the fact that

$$\frac{\partial \Theta}{\partial r} = 0 \quad \text{at } r = 0 \quad (22)$$

we obtain:

$$B = -\frac{4q}{c_p \rho R v_0} \quad (23)$$

where

$$q = -c_p \rho \kappa_0 (\partial \Theta / \partial r)_{r=R} \quad (24)$$

and the Reynolds number

$$Re = \frac{2}{v_0 R} \int_0^R u(r) r dr. \quad (25)$$

Using relations (23)–(25) the heat equation (21) can be written in the nondimensional form:

$$\frac{1}{r_*} \frac{\partial}{\partial r_*} \left(r_* x v_* \frac{\partial \Theta_*}{\partial r_*} \right) = -\frac{2u_*}{Re} \quad (26)$$

where $\Theta_* = \Theta / T_*$ and x is given by relation (14). The

parameter T_* is defined as follows:

$$T_* = \frac{q}{c_p \rho u_*}. \quad (27)$$

Using the above notation, the Nusselt number is given by

$$Nu = C_h \sigma_0 Re \quad (28)$$

where

$$C_h = R_*^2 / \left(2 \int_0^{R_*} \Theta_* u_* r_* dr_* \right).$$

To describe heat transfer in turbulence, one needs an expression for the coefficient of heat conductivity which takes into account both molecular and turbulent contributions to the heat transfer process. The theory leading to relation (14) determines the turbulent diffusivity in terms of the laminar transport coefficients and the turbulent viscosity. In particular, it describes the interaction between molecular and turbulent transport, an effect of much significance at low Re and σ_0 . Thus, the determination of turbulent heat transfer from (14) requires reliable data on turbulent viscosity. Such data can be found either from theory or from analysis of experimental data on velocity profiles in pipe flow.

In the present work we are interested exclusively in demonstrating the power of the 'universal' relation (14) provided the expression for turbulent viscosity is known. Thus, we adopt the *ad hoc* model [12] for the dimensionless total viscosity ν_* :

$$\nu_* = 1 + 0.41 y_* [1 - \exp(-y_*^2 / A^2)], \quad A = 26$$

when the distance to the wall $y_* < 50$. The turbulent viscosity for $y_* > 50$ is that derived from the differential $k-\bar{\epsilon}$ model of Yakhot and Orszag [5]. The model viscosity and mean velocity profiles obtained by integrating the equation of motion (19) using this viscosity are presented in Figs. 1 and 2. The friction coefficient λ defined by $\tau_* = \lambda \rho u_*^2 / 8$ so $\lambda = 32(R_* / Re)^2$ is plotted in Fig. 3. It is apparent that the agreement with experimental data is very good.

The equation of motion (19) and heat equation (26)

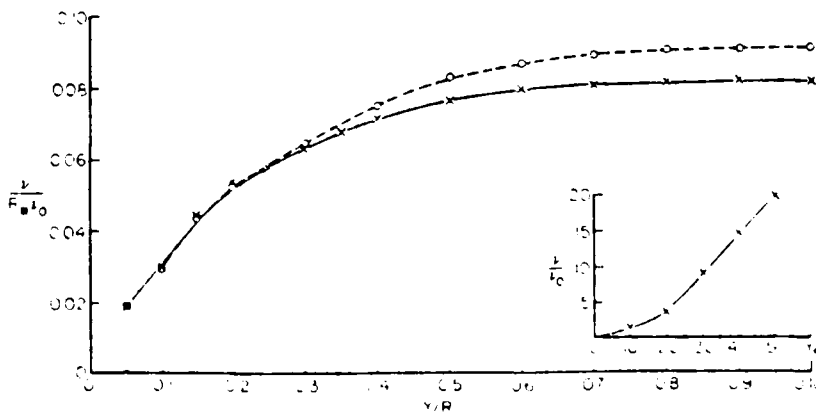


FIG. 1. Viscosity distribution in a pipe adopted in this work. \rightarrow $Re = 40,000$, $R_* = 346,000$.

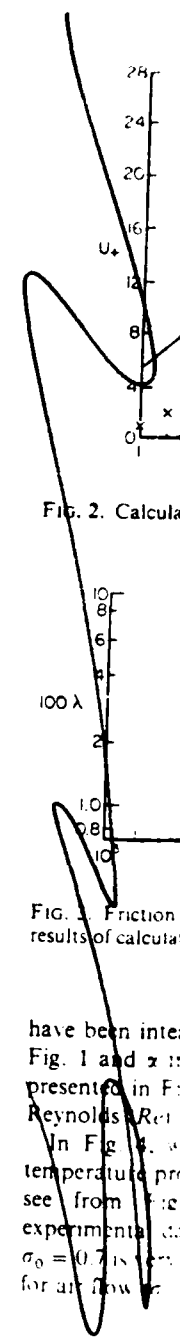


FIG. 2. Calculated friction results of calculated temperature profiles.

have been integrated numerically. The results are presented in Figs. 1 and 2. The Reynolds number $Re = 40,000$. In Fig. 3, the friction coefficient λ versus the dimensionless total viscosity ν_* is presented. The experimental data for air flow at $Re = 40,000$ and $\sigma_0 = 0.71$ is also shown for comparison.

FIG. 3. Friction coefficient λ versus dimensionless total viscosity ν_* .

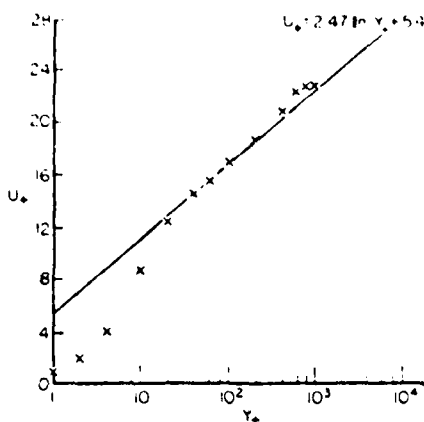


FIG. 2. Calculated dimensionless velocity profile.
 $u_* = u u_*$; $Re = 40.000$.

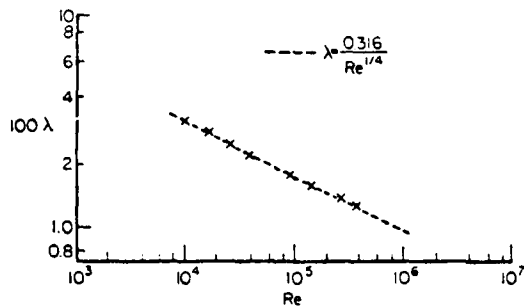


FIG. 3. Friction coefficient λ for turbulent pipe flow: \times results of calculation based on the model viscosity from Fig. 1; $--$ Blasius formula.

have been integrated using the model viscosity from Fig. 1 and α from the relation (14). The results are presented in Figs. 4-10 for various Prandtl (σ_0) and Reynolds (Re) numbers.

In Fig. 4, we plot the calculated and measured temperature profiles for air flow in a pipe. As we can see from Fig. 4, the agreement between the experimental data and the results of calculations for $\sigma_0 = 0.7$ is very good. The calculated Nusselt number for air flow ($\sigma_0 = 0.7$) is compared in Fig. 5 with the

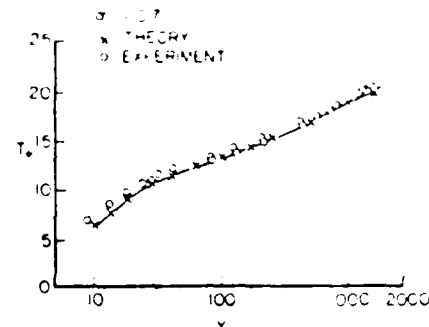


FIG. 4. Dimensionless temperature profile $T_* = T/T_0$. \times results of calculations, \circ experimental data [11].

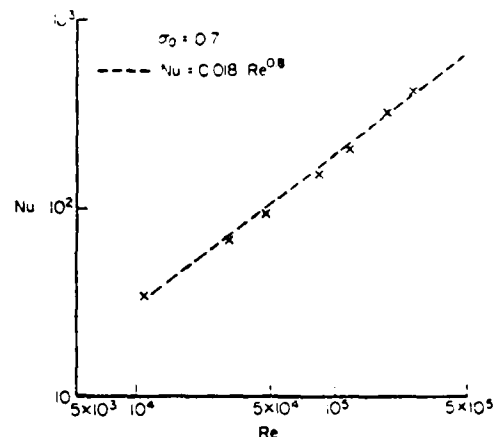


FIG. 5. Nusselt number Nu as a function of Reynolds number $Re = u_* D / \nu_0$ for the air flow ($\sigma_0 = 0.7$) in a pipe: \times results of calculations; $--$ empirical relation
 $Nu = 0.018 Re^{0.8}$.

empirical relation widely used in the literature [11]:

$$Nu = 0.018 Re^{0.8}. \quad (29)$$

The prediction of turbulent heat transfer in low-Prandtl-number flow is a most difficult test for the model. In Fig. 6, the calculated temperature profiles in liquid mercury ($\sigma_0 = 0.02$) and in the NaK eutectic ($\sigma_0 = 0.029$) are plotted for pipe flow at $Re = 149.000$

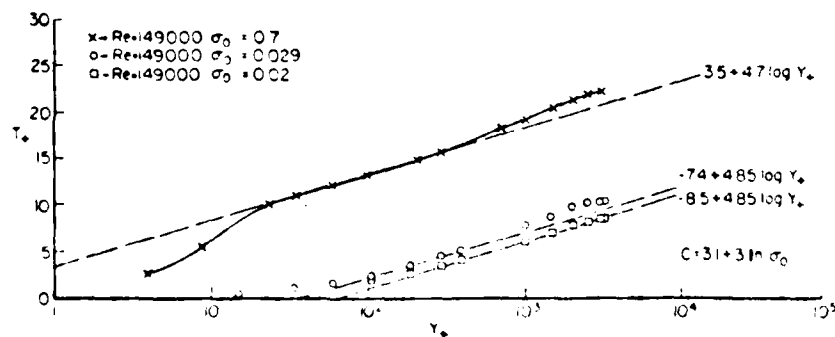


FIG. 6. Dimensionless temperature (T_*) profiles in turbulent flow in a pipe at $Re = 149.000$: \times air ($\sigma_0 = 0.7$); \circ NaK eutectic ($\sigma_0 = 0.029$); \square mercury ($\sigma_0 = 0.02$). — from ref [13].

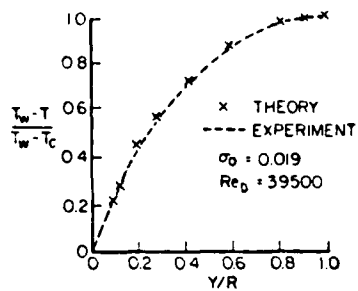


FIG. 7. Temperature defect $(T_w - T)/(T_w - T_c)$ distribution in turbulent flow in a pipe: x results of calculation for NaK eutectic ($\sigma_0 = 0.019$); --- experimental data of ref. [13].

It is apparent that some fraction of the temperature profile ($y_* = 100$) can be approximated by the logarithmic law:

$$T_* = C + 4.85 \log y_* \quad (30)$$

where the constant C can be found from the relation:

$$C = 3.1 + 3 \ln \sigma_0. \quad (31)$$

A relation very similar to (31) has been obtained from analysis of experimental data [11].

It should be mentioned that when the Prandtl number is small ($\sigma_0 = 0.02$) the logarithmic part of the temperature profile appears only at high Reynolds numbers: $Re > 10^5$. For $Re < 10^5$, no part of the temperature profile can be approximated by the relation (30).

The results of our calculations may be compared with the experimental data of Buhr *et al.* [13]. The temperature profile measured in the NaK eutectic flow ($\sigma_0 = 0.019$) at $Re \approx 4 \times 10^4$ is compared with the present results in Fig. 7. In Fig. 8, we plot calculated and experimental data for the temperature profiles in several low-Prandtl-number fluids at different Reynolds numbers in the range $3 \times 10^4 < Re < 3.5 \times 10^5$. Again, the agreement between the results of calculations and experimental data is very good.

The Nusselt number Nu is plotted as a function of the Peclét number $Pe = \sigma_0 Re$ in Fig. 9. At low Pe , the

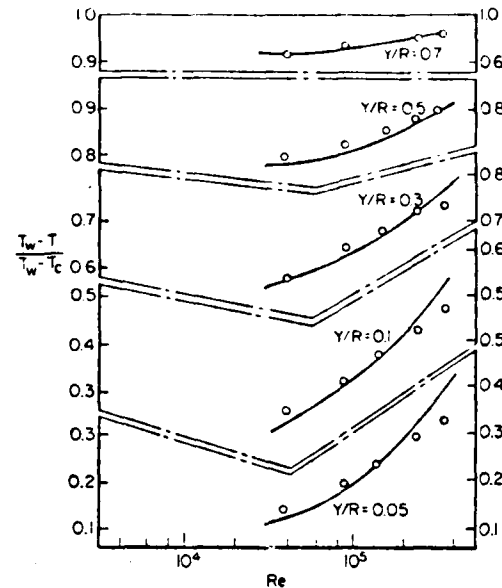


FIG. 8. Temperature defect $(T_w - T)/(T_w - T_c)$ distribution in turbulent flow in a pipe as a function of Reynolds number Re : \circ result of calculation; — experimental data of ref. [13].

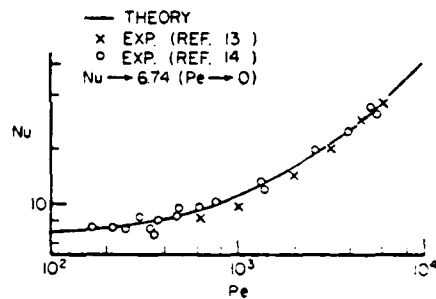


FIG. 9. Nusselt number Nu as a function of Peclét number Pe . $Nu \approx 6.74$ when $Pe \approx 0$.

results of numerical calculations give $Nu \approx 6.74$. This is very close to the experimentally observed [13, 14] limiting Nusselt number $Nu \approx 6.8-7.0$.

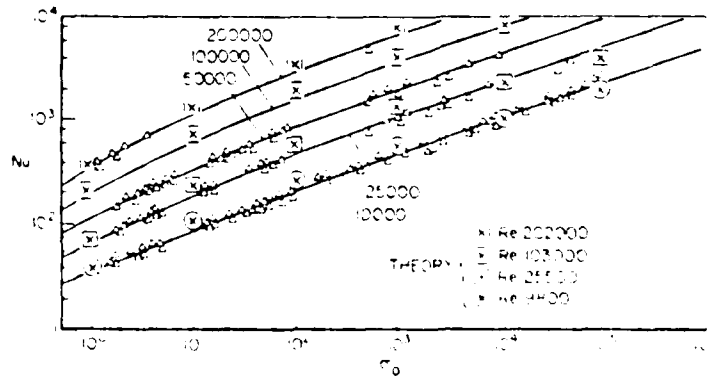


FIG. 10. Nusselt number Nu as a function of Prandtl number σ_0 . Experimental data are taken from ref. [11].

Another model for the prediction of heat transfer in very low Prandtl number fluids. In this case, entirely by calculation. Fig. 10. measurement of Prandtl number $2.5 \times 10^{-3} < \sigma_0 < 10^{-2}$. We conducted the accuracy throughout accessible orders of magnitude.

Acknowledgments. Naval Research Force Office 83-C-0026, MSM-8514! Contract DF

Note added development that the properties of physical dimensions powers of ϵ ratio modification and changes t

1. M. J. Rey (1975).
2. F. Gon. V. Heat Trans.
3. S. Aoki, A. J. J. J. J. Institute.
4. M. J. J. J. Institute.
5. V. Yakhot, D. Forster, J. Fluid Mech. 712 (1977).
6. P. C. Mar. Phys. 64 (1977).
7. V. Yakhot, J. Heat Trans. 99 (1977).
8. V. Yakhot, J. Heat Trans. 100 (1978).
9. V. Yakhot, J. Heat Trans. 101 (1979).
10. L. D. Landau, P. E. Lifshitz, "Statistical Physics," Butterworths, London, 1956.
11. A. S. Monin, "Dynamics of Turbulent Flow," Gostekhizdat, Moscow, 1959.
12. W. R. Reynolds, "Fluid Mechanics," Cambridge University Press, Cambridge, 1958.
13. H. O. Bingham, "Mechanics of Fluids," Macmillan, New York, 1960.
14. S. S. Kline, "Turbulent Flow in Pipe," McGraw-Hill, New York, 1955.

In this paper, we present a new model for the prediction of heat transfer in very low Prandtl number fluids. In this case, entirely by calculation. Fig. 10. measurement of Prandtl number $2.5 \times 10^{-3} < \sigma_0 < 10^{-2}$. We conducted the accuracy throughout accessible orders of magnitude.

Another test of both the relation (14) and of the model for turbulent viscosity adopted in this work is the prediction of heat transfer in high-Prandtl-number fluids. In this case, the molecular heat diffusivity is very low and the heat transfer process is determined entirely by the turbulent eddy diffusivity. The results of calculations are compared with experimental data in Fig. 10. The agreement with the results of measurements [11] is very good across a wide range of Prandtl and Reynolds numbers, $1 < \sigma_0 < 10^6$ and $2.5 \times 10^4 < Re < 2 \times 10^5$.

We conclude that the relation (14) can be used for the accurate description of turbulent heat transfer throughout the entire range of experimentally accessible Prandtl numbers, which vary over eight orders of magnitude, i.e. $10^{-2} < \sigma_0 < 10^6$.

Acknowledgement—This work was supported by the Office of Naval Research under Contract N00014-82-C-0451, the Air Force Office of Scientific Research under Contract F49620-85-C-0026, the National Science Foundation under Grant MSM-8514128 and the Department of Energy under Contract DE-AC0684ER13153.

Note added in proof—In more recent work on the development of the RNG method (see ref. [5]), we have found that the proper technique is to evaluate all constants at the physical dimension $d = 3$ to lowest order in an expansion in powers of ϵ rather than at the critical dimension $d = 7$. This modification changes the turbulent Prandtl number to 0.7179 and changes the results presented here by several percent.

REFERENCES

1. A. J. Reynolds, *Int. J. Heat Mass Transfer* **18**, 1055 (1975).
2. F. Gori, M. A. El Halidy and D. B. Spalding, *Numer. Heat Transfer* **2**, 441 (1979).
3. S. Aoki, *Bull. Tokyo Inst. Technol.* **54**, 63 (1963).
4. M. Jischka and H. B. Rieke, *Proc. Advanced Study Institute*, July 20, Istanbul (1978).
5. V. Yakhot and S. Orszag, *J. Sci. Comp.* **1**, 1 (1986).
6. D. Forster, D. Nelson and H. Stephen, *Phys. Rev.* **A16**, 732 (1977).
7. P. C. Martin and C. DeDominics, *Suppl. Prog. theor. Phys.* **64**, 108 (1978).
8. V. Yakhot, *Phys. Rev.* **A23**, 1486 (1981).
9. V. Yakhot and S. Orszag, In *Non-Linear Dynamics of Transcritical Flows* (Edited by H. L. Jordan, H. Oertel and K. Robert), p. 155. Springer, Berlin (1985).
10. L. D. Landau and E. M. Lifshitz, *Fluid Mechanics*. Pergamon Press, Oxford (1982).
11. A. S. Monin and A. M. Yaglom, *Statistical Fluid Dynamics*, Vol. 1. MIT Press, Cambridge, MA (1971).
12. W. Reynolds, Computation of turbulent flows, *A. Rev. Fluid Mech.* **8**, 183 (1976).
13. H. O. Buhr, A. D. Carr and R. E. Balshier, *Int. J. Heat Mass Transfer* **11**, 641 (1968).
14. S. S. Kutateladze, *Osnovy Teorii Teploobmena* (in Russian). Nauka, Novosibirsk (1970).

APPENDIX

In this Appendix we will introduce the scale elimination procedure leading to renormalization of molecular viscosity ν_0 and molecular diffusivity κ_0 . Using the incompressibility condition we write the equations of motion for the Fourier

components of velocity $v_i(k)$ and passive scalar $T(k)$ as (see refs. [8, 9])

$$v_i(k) = G^0(k)v_i(\hat{k}) + \frac{i}{2}G^0(k)P_{mn}(k) \int v_m(\hat{q})v_n(\hat{k}-\hat{q}) \frac{d\hat{q}}{(2\pi)^{d-1}}, \quad (A1)$$

$$T(k) = -i\nu_0(k)k \int v_i(\hat{q})T(\hat{k}-\hat{q}) \frac{d\hat{q}}{(2\pi)^{d-1}}, \quad k = (\hat{k}, \omega) \quad (A2)$$

where d is the dimensionality of the space

$$G^0(k) = (1 - i\nu_0 + \kappa_0 k^2)^{-1} \quad (A3)$$

$$g^0(k) = (1 - i\nu_0 + \kappa_0 k^2)^{-1} \quad (A4)$$

and the random force f is given by the correlation function

$$\langle v_i(\hat{k})v_j(\hat{k}') \rangle = (2\pi)^{d-1} 2D_v(k) \delta(\hat{k}-\hat{k}') \quad (A5)$$

The projection operator P_{mn} is defined as $P_{mn}(k) = k_m P_{mn}(k) + k_n P_{mn}(k)$. Here $i = 3$ and $D_v(k) =$

The equations of motion (A1) and (A2) are defined on the domain $0 < k < \Lambda$. The RNG procedure consists of two steps. First, we write equations in terms of the velocity field decomposition on two components $v_i^<(k)$ and $v_i^>(k)$ defined on the intervals $\Lambda e^{-1} < k < \Lambda$ and $0 < k < \Lambda e^{-1}$, respectively ($\lambda_0 = 1$):

$$v_i(k) = G^0(k) - \frac{i\nu_0}{2}G^0P_{mn}(k) \int [v_m^<(\hat{q})v_n^<(\hat{k}-\hat{q}) + 2v_m^<(\hat{q})v_n^<(\hat{k}-\hat{q}) - v_m^>(\hat{q})v_n^>(\hat{k}-\hat{q})] \frac{d\hat{q}}{(2\pi)^{d-1}} \quad (A6)$$

$$T(k) = -i\lambda_0 k_1 g^0(k) \int [v_i^<(\hat{q})T^<(\hat{k}-\hat{q}) - v_i^>(\hat{q})T^>(\hat{k}-\hat{q}) + v_i^<(\hat{q})T^>(\hat{k}-\hat{q}) + v_i^>(\hat{q})T^>(\hat{k}-\hat{q})] \frac{d\hat{q}}{(2\pi)^{d-1}} \quad (A7)$$

In order to eliminate modes from the interval $\Lambda e^{-1} < k < \Lambda$, all terms $v_i^>(k)$, $T^>(k)$ should be removed by repeated substitution of (A6) for $v^>$, $T^>$ back into (A6). This generates infinite expansions for $v^<$, $T^<$ in powers of λ_0 in which $v^>$, $T^>$ do not formally appear. Next, averages are taken over the part of the random force f belonging to the strip $\Lambda e^{-1} < k < \Lambda$. This procedure formally eliminates the modes $\Lambda e^{-1} < k < \Lambda$ from the problem.

It follows from (A6) that, after removing the modes $\Lambda e^{-1} < k < \Lambda$, the equation of motion for $v^<$, $T^<$ can be written up to second order in λ_0 as:

$$\begin{aligned} (-i\nu_0 + \kappa_0 k^2)v_i^<(k) &= f_i(k) - \frac{i\lambda_0}{2}P_{mn}(k) \int f_m^>(\hat{q})f_n^>(\hat{k}-\hat{q}) \frac{d\hat{q}}{(2\pi)^{d-1}} - \frac{i\lambda_0}{2}P_{mn}(k) \\ &\times \int v_m^<(\hat{q})v_n^<(\hat{k}-\hat{q}) \frac{d\hat{q}}{(2\pi)^{d-1}} - 4\left(\frac{i\lambda_0}{2}\right)^2 2D_v(k)P_{mn}(k) \\ &\times \int |G^0(\hat{q})|^2 G^0(\hat{k}-\hat{q})P_{mn}(k-q)q^{-2}v_q(\hat{k}) \frac{d\hat{q}}{(2\pi)^{d-1}} \\ &+ O(\lambda_0^3). \end{aligned} \quad (A8)$$

The equation for $T^<(k)$ is:

$$\begin{aligned} (-i\nu_0 + \kappa_0 k^2)T^<(k) &= -i\lambda_0 k_1 \int v_i^<(\hat{q})T^<(\hat{k}-\hat{q}) \frac{d\hat{q}}{(2\pi)^{d-1}} - 2\lambda_0^2 D_v(k)T^<(k)k_1 \\ &\times \int |G^0(\hat{q})|^2 g^0(\hat{k}-\hat{q})P_{mn}(q) \frac{d\hat{q}}{(2\pi)^{d-1}}. \end{aligned} \quad (A9)$$

When the $O(\lambda_0^3)$ terms on the RHS of (A7) and (A8), which are $O(k^3 v)$ and $O(k^2 T)$, respectively, are moved to the LHS, it gives corrections to the bare viscosity $\nu_0 k^2$ and diffusivity $\kappa_0 k^4$:

$$\Delta v = A_1 \frac{\lambda_0^2 D_v \epsilon^{d-1}}{18 \lambda_0^4 - \epsilon}$$

and

$$\Delta\lambda = K_d \frac{\lambda_0^2 D_0}{\nu_0(\kappa_0 + \nu_0)} \frac{e^d - 1}{d}$$

where

$$\epsilon = 4 + y - d$$

$$A_d = \frac{d^2 - d - \epsilon}{2d(d+2)} \frac{S_d}{(2\pi)^d}$$

$$K_d = \frac{d-1}{d} \frac{S_d}{(2\pi)^d}; \quad S_d = \frac{2\pi^{d/2}}{\Gamma(d/2)}$$

The parameter $d = 7$ at the fixed point. Thus, elimination of small scales leads to renormalization of viscosity and diffusivity. The second step of the procedure consists of iterating the scale-elimination procedure. This leads to the results given in Section 2.

TRANSFERT THERMIQUE DANS LES ECOULEMENTS TURBULENTS— I. ECOULEMENT DANS UN TUBE

Résumé—L'expression du nombre de Prandtl turbulent obtenue à partir d'une procédure de groupe de renormalisation est utilisée pour décrire le mécanisme du transfert thermique dans l'écoulement turbulent dans un tube. Les résultats sont en bon accord avec des données expérimentales dans le domaine des nombres de Prandtl $10^{-2} < \sigma_0 < 10^6$ accessibles expérimentalement.

WÄRMEÜBERGANG IN TURBULENTEN FLUIDEN—I. ROHRSTRÖMUNG

Zusammenfassung—Zur Beschreibung des Wärmeübergangs bei turbulenter Rohrströmung wird der Ausdruck für die turbulente Prandtl-Zahl verwendet, den man aus der Renormalisations-Gruppen-Prozedur erhält. Die Ergebnisse stimmen mit experimentellen Daten im gesamten Bereich der experimentell verfügbaren Prandtl-Zahlen, $10^{-2} < \sigma_0 < 10^6$, gut überein.

ТЕПЛОПЕРЕНОС В ТУРБУЛЕНТНЫХ ЖИДКОСТЯХ. ТЕЧЕНИЕ В ТРУБЕ

Аннотация—Для описания теплопереноса при турбулентном течении в трубе используется выражение для турбулентного числа Прандтля, полученное методом ренормализационной группы. Результаты находятся в хорошем соответствии с экспериментальными данными для всего диапазона значений числа Прандтля, $10^{-2} < \sigma_0 < 10^6$.

Aber
expere
combi
natu
heat
combi

COMBINED
vertical flat
heat transfer
A number of
to investiga
However, m
combined c
was obtaine
This is main
combined flo
high Rayleig
and such exp
in a laborato
experimental
of turbulent f
Hall and P
on an ascen
conviction ov
They found :
regime, initial
forced flow
Suggest the
combined eq.
use for furthe
coefficients n
has performe
turbulent con
buoyancy, for
accounted for
it is uncertain
transfer behav
the relevant e
not been avail

Hall and P
on an ascen
conviction ov
They found :
regime, initial
forced flow
Suggest the
combined eq.
use for furthe
coefficients n
has performe
turbulent con
buoyancy, for
accounted for
it is uncertain
transfer behav
the relevant e
not been avail

On the other
the turbulent
been conduct

NUMERICAL SIMULATION OF TURBULENT SPOTS
IN CHANNEL AND BOUNDARY LAYER FLOWS

By

Edward T. Bullister

*Department of Mechanical Engineering,
Massachusetts Institute of Technology,
Cambridge, Mass. 02139*

AND

Steven A. Orszag

*Department of Applied and Computational Mathematics,
Princeton University, Princeton, New Jersey 08544*

Abstract

The initiation and early growth of spots in channel and boundary layer flows is simulated using a three dimensional spectral code. The simulated spots show significant agreement with available experimental data for such quantities as growth rates and spreading angles. Disturbances are introduced into the center and edge of the developing channel spots to investigate the relative sensitivity of spots.

1. INTRODUCTION

Emmons¹ was the first to observe turbulent spots in a laminar flow undergoing transition to a turbulent flow. Since then a large number of investigators have recognized the importance of spots in the study of both transition and turbulence. Naturally occurring spots are initiated by flow disturbances like noise. In the laboratory, spots may be artificially initiated with electric sparks or by injecting a jet of fluid. In a numerical simulation of spots, controlled disturbances may be imposed on a solution of the Navier-Stokes equations.

Soon after Emmons' discovery, Elder² noted that spots tend to grow independently of one another, even when they overlap. Gaster^{3,4} studied the linear growth of small amplitude disturbances into a wave packet using both laboratory experiments and theoretical analysis. His theoretical predictions have been confirmed by laboratory observations so long as nonlinear effects are not important. Wygnanski, Sokolov, and Friedman⁵ conducted an experimental study of spots in a boundary layer. Using conditional sampling techniques, they mapped out the geometry and growth rates of a spot as it develops in a boundary layer. Gad-el-Hak, et al.⁶ conducted flow visualization experiments on boundary layer spots by injecting dye upstream of the spot initiation. They divided the spot into five regions(see Figure 1). Region I within the spot overhangs region II,

the laminar boundary layer below the head of the spot. Region III appears similar to a turbulent boundary layer. In regions IV and V the flow returns to a "calm" state. The photograph in Figure 2 illustrates the characteristic arrowhead shape of a boundary layer spot in streamwise-spanwise projection. This photograph was obtained by illuminating dye lines with a sheet of light very close to the wall.

The first detailed research directed toward investigating the characteristics of spots in a channel was conducted by Carlson, et al.⁷ Using mica flakes to visualize the flow (Figure 3), they observed that a channel spot also has the characteristic arrowhead shape. They identified (see Figure 4) several features present in channel spots. The spreading half-angle (1) was about 8 degrees. The leading edges met at a sharp point and were preceded by oblique waves(7). The center of the spot (4) contained small scale turbulence. Streaks(3) trailed from region 4.

The purpose of the present study is to use direct numerical solution of the Navier-Stokes equation to identify details of the internal structure of spots, as well as to map out spot dimensions and growth rates. Comparison of our results for growth rates of the large-scale spot dimensions with those seen experimentally verifies that the essential growth mechanisms of spots is captured by our numerical experiments.

One previous study of numerical spots should be mentioned. Leonard⁸ used discrete vortex methods to simulate numerically the early growth of a spot in a boundary layer. As with the present computations, the spots computed by Leonard are typically less mature than experimentally observed spots.

2. COMPUTATIONAL GEOMETRIES AND NUMERICAL METHODS

The computational domain that we use to simulate channel flow spots is as follows. In our simulations of channel flow spots, the flow is represented by $128 \times 64 \times 33$ Fourier and Chebyshev modes in the x (streamwise), y (spanwise), and z (normal) directions, respectively (see Figure 5). The flow satisfies periodic boundary conditions in x and y and no-slip (rigid) boundary conditions at the walls ($z=\pm 1$). The computational box is nondimensionalized by the channel half-width; in the runs presented below, the physical box size is $20 \times 5 \times 2$. With 128×64 resolution in x and y , the resultant node spacing (in physical space) of the spectral collocation points is $\Delta x=0.16$ and $\Delta y=0.08$.

For our boundary layer spot calculations, the flow is represented using 64 Fourier modes in x and y , with $\Delta x=2$ and $\Delta y=1$ (see Figure 6). In the z direction, the 33 collocation points are obtained by an algebraic mapping of the interval $[-1,1]$ to $[0,\infty]$ with half the collocation points located in the region $0 < z < 5$. The computational box is nondimensionalized by the boundary layer thickness $\eta = \sqrt{\nu x_0 / U_\infty}$ at some representative x -location x_0 . The periodic boundary conditions used in the streamwise direction are only approximate. They are justified because the increase in boundary layer thickness through the computational domain is only 6% (see also Balasubramanian, et al⁹). While inflow-outflow boundary conditions are, in principle, more realistic than periodic boundary conditions, they are more

wasteful of spatial resolution, which is the limiting factor in the present calculations.

The Navier-Stokes equations are solved in rotational form,

$$\frac{dv}{dt} = v \times \omega - \nabla(\Pi) + 1/Re \nabla^2(v)$$

$$\nabla \cdot (v) = 0$$

where $\omega = \nabla \times v$ is the vorticity and $\Pi = P + v^2/2$. The velocities are normalized with respect to the centerline velocity in the channel and the free stream velocity in the boundary layer.

The spectral method of Orszag and Patera¹⁰ is used in both the channel and boundary layer calculations. For the boundary layer, the scheme is modified by mapping the Chebyshev collocation points of the channel to the desired locations in the boundary layer. A mapping function

$$z^* = f(z)$$

is chosen. When taking derivatives in the z-direction (e.g., in calculating the vorticity) the Chebyshev differentiation in z^* is followed by multiplication by $f'(z)$:

$$\frac{d}{dz} = \frac{df}{dz} \frac{d}{dz^*}$$

The boundary condition at infinity ($v_x = 1$) is implemented by recalculating the (0,0) Fourier mode (the mean flow in x and y) in the viscous step. Symmetry is not imposed, but the spots develop symmetrically when symmetric initial conditions are used.

The disturbance is initiated by applying a body force to a packet of fluid, producing a small jet normal to and away from the wall. The form of the disturbance is Gaussian in x and y and continuous in time.

$$F = G(t) e^{[-r^2/2\sigma^2]}$$

where $G(t)$ is a ramp function. The size of the jets are indicated in Table I.

TABLE I

	Channel	B.L.
σ	0.16	0.7
Location	$0.1 < z < 0.2$	$0.05 < z < 1.5$
Peak normal		
Velocity	0.09	0.035

We impose the following boundary conditions on the flow through the channel: the velocity at the walls is zero, and the flow is periodic at the inflow/outflow and cross-stream

boundaries. The Reynolds number for the channel runs is 6000 based on the channel half-width. The Reynolds number for the boundary layer simulations is 1000 based on the boundary layer thickness corresponding to $\eta=1.0$.

3. SPOTS IN CHANNEL FLOWS

In Figure 7, we plot contours of the maximum (in y) of the absolute value of the normal velocity, $\text{Max}_y |v_z|$ for a channel spot at $Re=6000$. The contour plots we present for channel spots encompass the entire $20 \times 5 \times 2$ computational domain; their dimensions are not to scale. Except where noted, the contours are at 1% intervals of $\text{Max}_q |v_z|$, where q is the coordinate normal to the plotting plane. With this projection of the spot onto a plane we view the data from the experimentalist's perspective (with the line of sight extending all the way through the channel). At time $t=1$, the initial disturbance has convected downstream and has become slightly distorted. The initial peak velocity of 0.09 has decreased to 0.038 due to viscous diffusion. By a time of $t=3$, the velocity has increased to 0.05 due to instability in the flow. The disturbance is elongated in x as well as convected downstream. In Figure 8 we see the disturbance develop most of the features characteristic of a spot. The front of the disturbance moves away from the wall. The disturbance grows in all directions and the "arrowhead" shape becomes apparent. The peak normal velocity increases from 6% at $t=12$ to 9% at $t=18$.

In Figure 9 we show the development of the boundaries with an isometric view. Enclosed within the surface is fluid whose x velocity differs from the Poiseuille profile by more than 2%.

The results plotted in Figure 10 are $\text{Max}_y |v_z|$ and $\text{Max}_z |v_z|$. At $t=30$, the spot has fully extended through the channel with a peak normal velocity of 13%. The initial disturbance on the bottom wall has induced a new disturbance at the top wall. This second, smaller spot has a peak velocity that occurs at a distance of approximately 0.25 (1/8 channel width) away from the top wall. By $t=30$, the two spots have joined to produce a disturbance that fills the span of the channel.

In Figure 11 we show the distortion of the Poiseuille profile at the spot center. The velocity at the edge is essentially unchanged from that of the original Poiseuille flow, while at the spot center there is a velocity defect of 0.1-0.2. At the bottom wall, the shear has increased by a factor of 3.

In Table II and Figure 12, we show how the spot geometry changes in time. Although there are significant differences between conditions generating our numerical spot and those generating the spots studied experimentally, a comparison of numerical and laboratory features is instructive. Carlson et al⁸ generated spots in a laboratory channel flow at $Re=1000$, while we used $Re=6000$ in our calculations. Most of the experimental data were taken more

than 50-100 channel widths downstream of the initial disturbance, while we have been able to follow the spot for only 10 channel widths. Further development of the channel spot would require a larger computational domain. The growth rate of the width and length of the numerical spot becomes constant at $t=15$ and remains so until the spot fills the domain at $t=32$. This steady growth rate is slightly higher than that observed experimentally in both the lateral and longitudinal directions. This discrepancy can be due to the difference in Reynolds numbers or to the lack of maturity of our computed spots compared to those studied experimentally. We have not observed in our data any significant evidence of the leading Tollmien-Schlichting waves that were observed experimentally. Again, we believe that the absence of these waves is due to the lack of maturity of our computed spots.

Table II Channel Spots

	Experimental		Computational
Velocity of Front	0.6		0.85
Rear	0.34		0.25
Spreading Half-Angle	8°		10°

A further numerical calculation was done to compare the stability characteristics of the spot at its edge and center. The velocity field of a spot at $t=20$ is used as the initial condition for three runs. The first run consists of restarting the original spot calculation and allowing the spot to continue development undisturbed to a time of 24. For the second run, a disturbance is applied at $t=20$ to the original spot at its center. This disturbance is of the same spatial and temporal extent as the original disturbance that initiated the spot, but the magnitude is $1/10$ that of the original. The difference between the resulting velocity fields, $\epsilon(x,t) = |v_{z1} - v_{z2}|$, is a measure of the effect of the disturbance. By $t=24$, $\epsilon(x,t)$ has exceeded 1% in the central $2/3$ of the spot (Figure 13). The third run is identical to the second, but with the disturbance applied at the spot edge, rather than at the center. At $t=24$ the disturbance had propagated through most of the spot (see Figure 14), and had a peak magnitude of about 4%, as opposed to the 1.5% peak from the second run.

From these results, we conclude that channel spots are less stable at their edges than at their centers. This observation suggests that spots grow by destabilization of neighboring fluid, rather than simply engulfing laminar fluid.

4. SPOTS IN BOUNDARY LAYER FLOWS

In Figures 15 through 17 we show the development of a boundary layer spot at $Re=1000$ up to $t=90$. The contour plots we present for boundary layer spots encompass the entire 128×64 computational domain in x and y and are truncated at $z=22$. Again, except where noted, the contours are at 1% intervals of $\text{Max}_q |v_z|$, where q is the direction normal to the plotting plane. Figure 15 shows the streamwise and spanwise development of the spot from the initial disturbance. At $t=90$, the spot has begun to develop the characteristic arrowhead shape, which is more apparent in the second (2%) velocity contour. Figure 16 shows the development of the triangular shape and the overhang in the spanwise direction. Figure 17 shows the overhang develop in the leading edge.

Table III Boundary Layer Spots

	Experimental		Computational
Velocity of Front	0.9		0.85
Rear	0.5		0.3
Spreading Half-Angle	10°		12°

The growth and development of the spot in a boundary layer is compared with the experimental findings of Wygnanski, et al⁵ in Table III. The growth rate of the spot

in the streamwise and spanwise directions is in relatively close agreement with the experimental data. This suggests that the growth mechanisms in a boundary layer spot have been accurately captured in this simulation.

Figure 18 shows cross sections of the spot at $t=90$. Here we plot contours of the local values of v_z at $y_{center} = 0.5, 2.5,$ and 4.5 , in Figures 18a, 18b, and 18c, respectively. Intervals are at 1% and dashed contour lines represent negative z velocities. The velocities are highest in the plane closest to the center of the spot (see Figure 18a). Away from the spot centerline the velocities and the spot height decrease. The front of the spot has an overhang of a distance of 10-20 in x , as has been observed experimentally. The flow is dominated by eddies with length scales of approximately 10 in x and 5 in y . These length scales differ from those of unstable modes of the Orr-Sommerfeld equations, which predicts linear instability for much longer wavelengths, $30 < \lambda_x < 85$.

In order to explore the later time evolution of boundary layer spots, it will be necessary to use higher resolution simulations, which we hope to perform in the future.

CONCLUSIONS

It has been shown that spots can be generated by numerical solution of the Navier-Stokes equations. The fact

that our results for the growth rates of the large-scale spot dimensions are relatively close to those seen experimentally suggests that the essential growth mechanisms of spots have been captured by our numerical experiments. These simulated spots are less mature than typical experimental spots, but their behavior appears to approximate that in a fully developed spot.

The spots generated were not dominated by two dimensional Tollmien-Schlichting waves. This suggests that the growth in spots is not linear growth of two dimensional Tollmien-Schlichting waves. Moreover, the perturbation velocities seen were about 0.1; perturbations this large would make the results of linear theory inapplicable and suggest domination of nonlinear effects. This does not rule out the importance of Tollmien-Schlichting waves in the amplification of small disturbances which may develop into spots or as a driving mechanism for some secondary instability in spots.

References

- ¹H. W. Emmons, J. Aero. Sci. 18, 490(1951).
- ²J. Elder, J. Fluid Mech. 9, 235(1960).
- ³M. Gaster and I. Grant, Proc. Royal Soc. 347, 253(1975).
- ⁴M. Gaster, 1975 Proc. R. Soc. Lond. 347, 271(1975).
- ⁵I. Wygnanski, M. Sokolov, and D. Friedman, J. Fluid Mech. 78, 785(1976).
- ⁶M. Gad-el-Hak, R. Blackwelder, and J. Riley, J. Fluid Mech. 110, 73(1981).
- ⁷A. Leonard, The Role of Coherent Structures in Modelling Turbulence and Mixing (ed. J. Jimenez). Lecture Notes in Physics, vol. 136, pp. 119-145. Springer(1981).
- ⁸D. R. Carlson, S. E. Widnall, and M. F. Peeters, J. Fluid Mech. 121, 487(1982).
- ⁹R. Balasubramanian, S. Orszag, A. M. Cary, J. Lin, M. Walsh Submitted to the J. Fluid Mech.
- ¹⁰S. Orszag and A. T. Patera, J. Fluid Mech. 128, 347(1983).

FIG. 1 Schematic of an experimental boundary layer spot cut through the center (from Gad-el-Hak et al.⁶).

FIG. 2 Visualization of an experimental boundary layer spot using fluorescent dye and a sheet of laser light at the wall; $Re_x = 5 \times 10^5$ (from Gad-el-Hak et al.⁶).

FIG. 3 Visualization of an experimental channel spot using mica platelets (from Carlson et al.⁸).

FIG. 4 Channel spot schematic: (1) spreading half angle; (2) trailing streaks; (3) region of small-scale turbulence (4) oblique Tollmien-Schlichting waves (from Carlson et al.⁸).

FIG. 5 Channel geometry and nomenclature. Channel is 20x5x2 in the x,y, and z directions, with 128x64 Fourier modes in x and y and 33 Chebyshev modes in z.

FIG. 6 Boundary layer geometry and nomenclature. Boundary layer computational domain is 128x64 in the x and y directions, with 64x64 Fourier modes in x and y and 33 Chebyshev modes mapped in the normal(z) direction.

FIG. 7 Early-time evolution of channel spot. $\text{Max}_y |v_z|$ contours are plotted at 1% intervals.

FIG. 8 Channel spot at intermediate times. $\text{Max}_z |v_z|$ contours in a) and b); $\text{Max}_y |v_z|$ contours in c) and d).

FIG. 9 Surfaces of 2% x-velocity perturbations in developing channel spot.

FIG. 10 Channel spot at $t=30$. $\text{Max}_z |v_z|$ contours in a); $\text{Max}_y |v_z|$ contours in b).

FIG. 11 Mean velocity profiles at center (solid) and edge (broken) of spot.

FIG. 12 Location in x of front, center, and rear of channel spot vs. time, where spot is defined as region where $|v_z| \geq 2\%$. For t larger than 30, the spot length reaches the periodicity length of the computational domain, so the spot ceases to grow in the streamwise direction.

FIG. 13 Perturbation velocity, $\epsilon(x,t)$, contours at $t=22$ and $t=24$ for channel spot perturbed at its center at $t=20$.

FIG. 14 Perturbation velocity, $\epsilon(x,t)$, contours at $t=22$ and $t=24$ for channel spot perturbed at its edge at $t=20$.

FIG. 15 Development of boundary layer spot. $\text{Max}_z |v_z|$ contours are plotted at 1% intervals. a) $t=30$; b) $t=60$; c) $t=90$

FIG. 16 Development of boundary layer spot. $\text{Max}_y |v_z|$ contours are plotted at 1% intervals. a) $t=30$; b) $t=60$; c) $t=90$

FIG. 17 Development of boundary layer spot. $\text{Max}_x |v_z|$ contours are plotted at 1% intervals. a) $t=30$; b) $t=60$; c) $t=90$

FIG. 18 Slices of spot at $t=90$. Contours of v_z at $y=32$, 30, and 28. The plane of symmetry of the spot is at $y=32.5$. Dotted lines represent negative v_z .

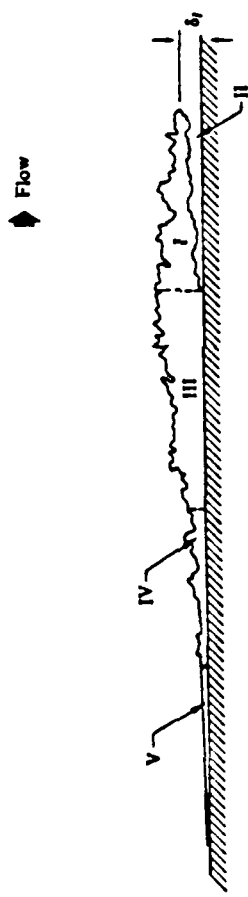


Figure 1

Figure 2

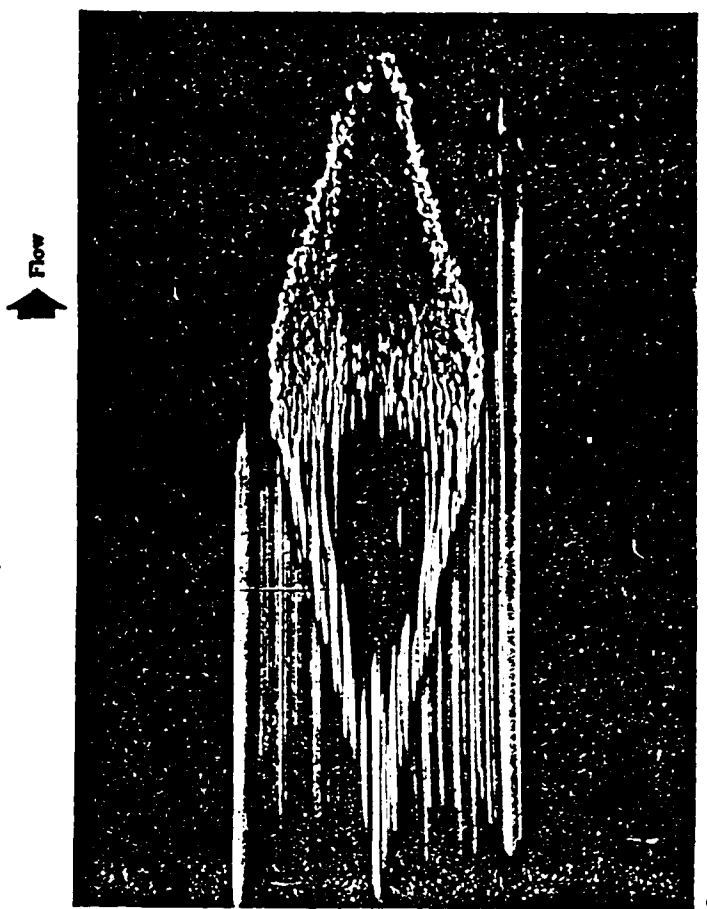


Figure 3



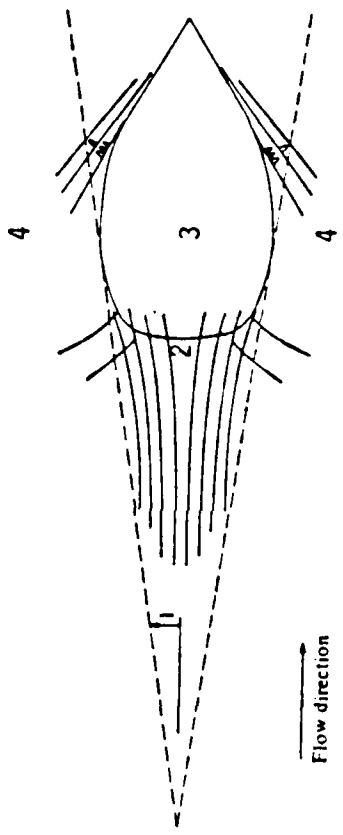


Figure 4

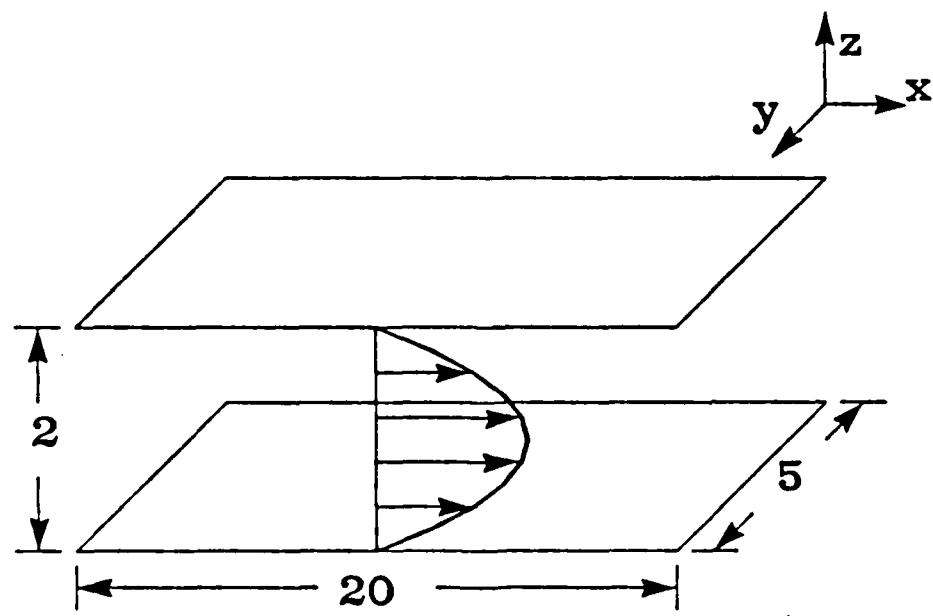


Figure 5

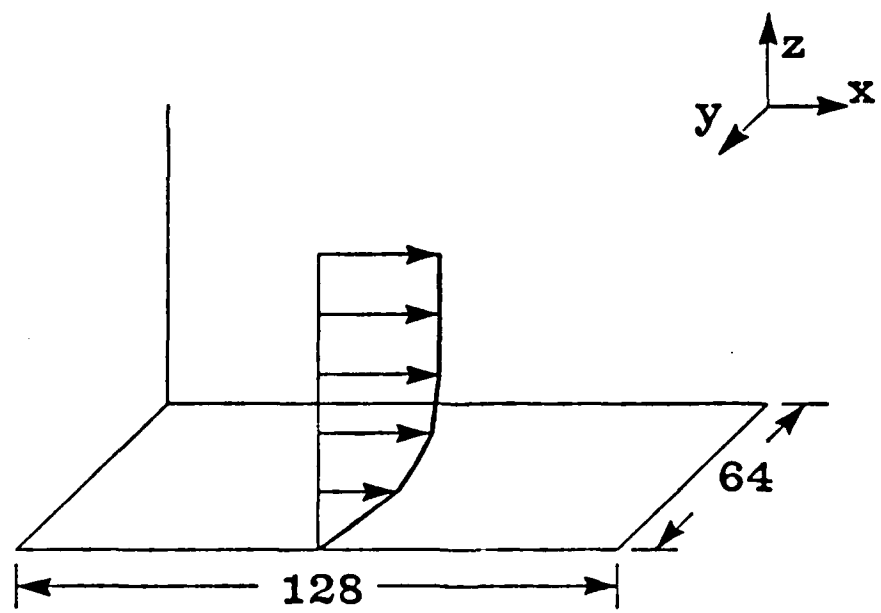
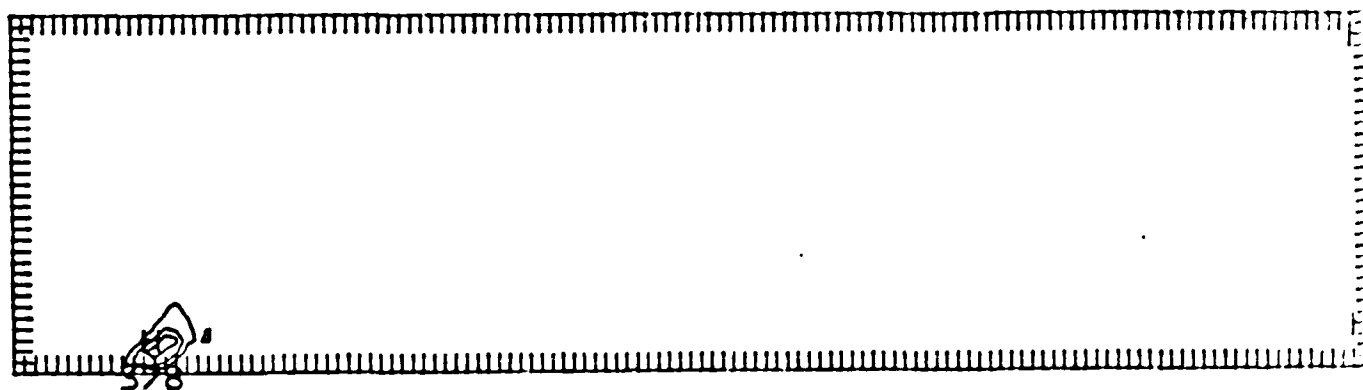


Figure 6

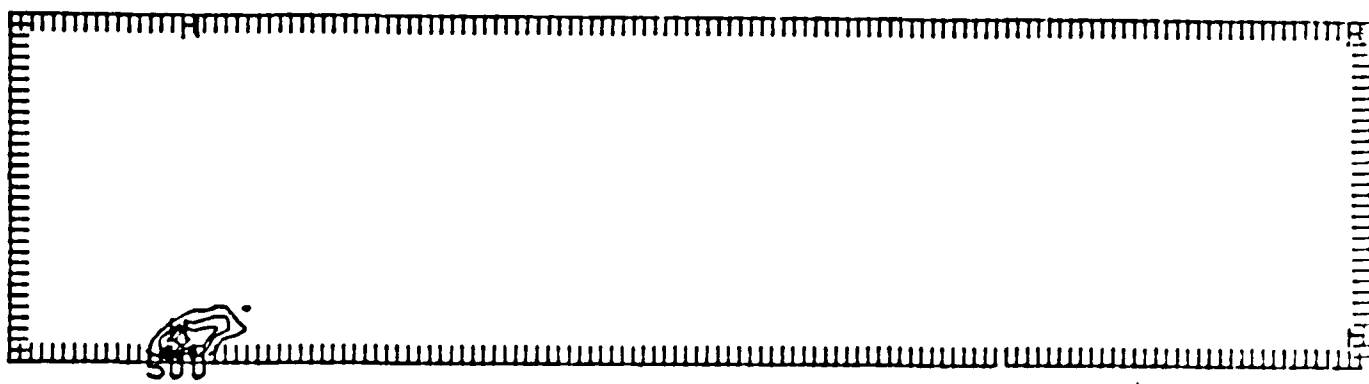
Early-Time Spot Evolution at R = 6000

TIME

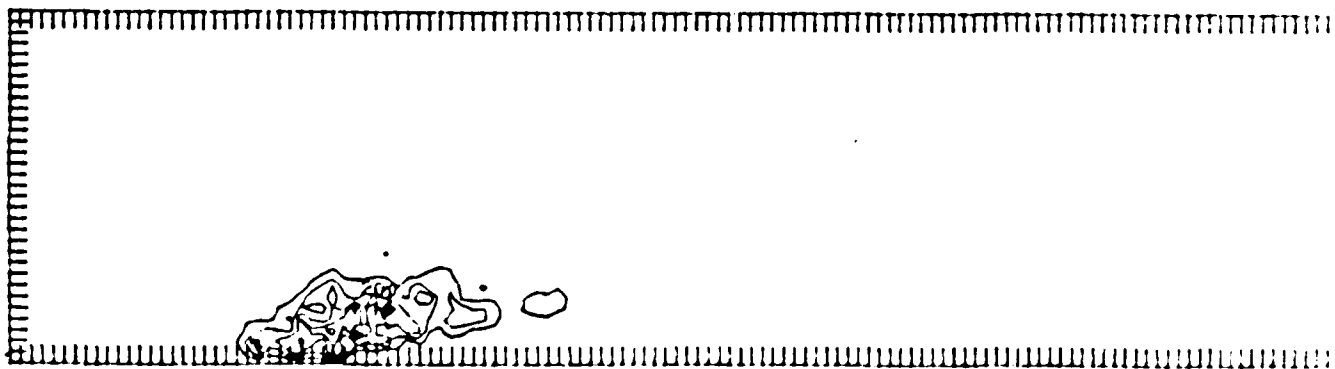
1



3



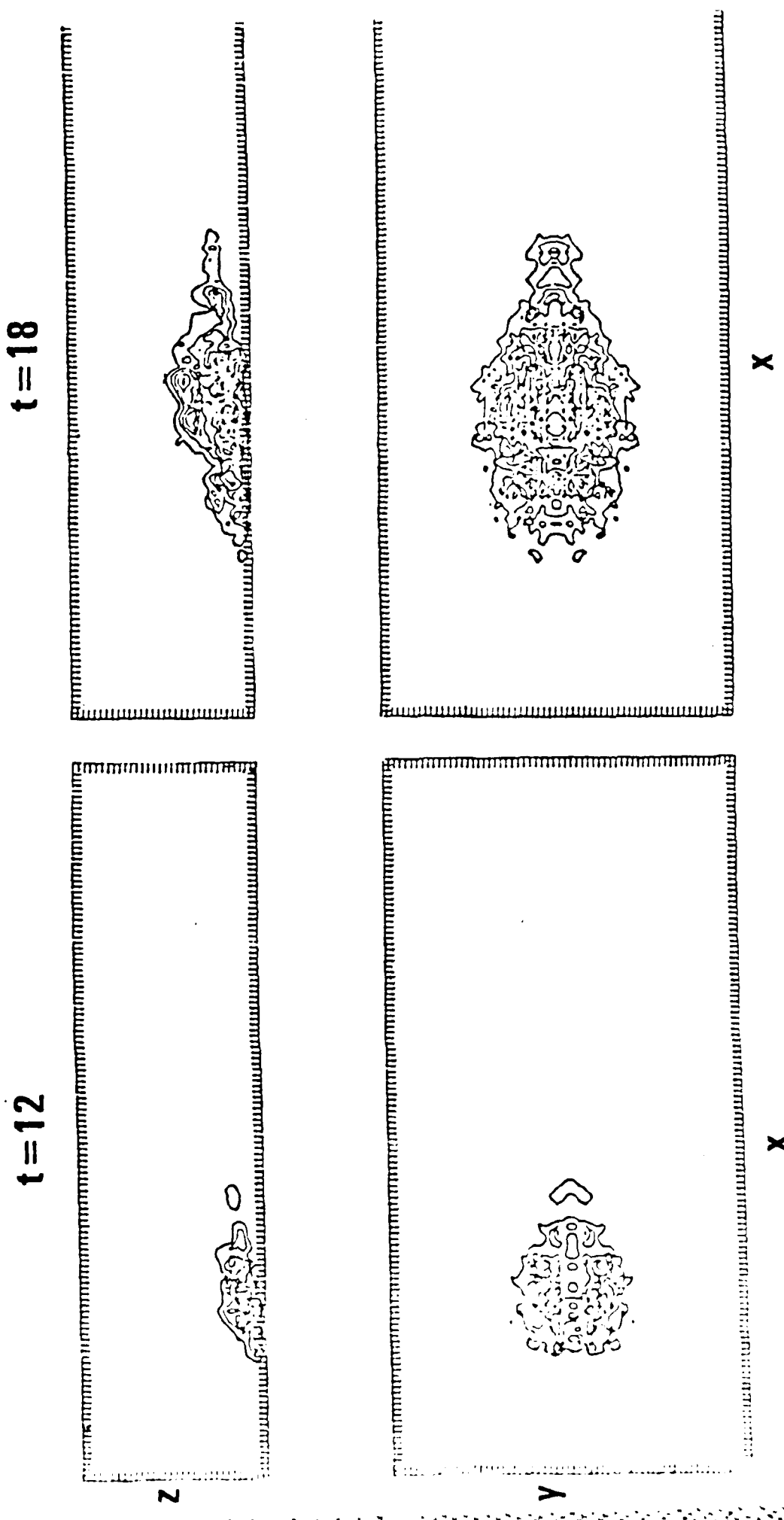
6



CONTOUR FROM 0.00000 TO 0.0000E+01

Figure 7

Figure 8



Surfaces of 2% x-Velocity Perturbation

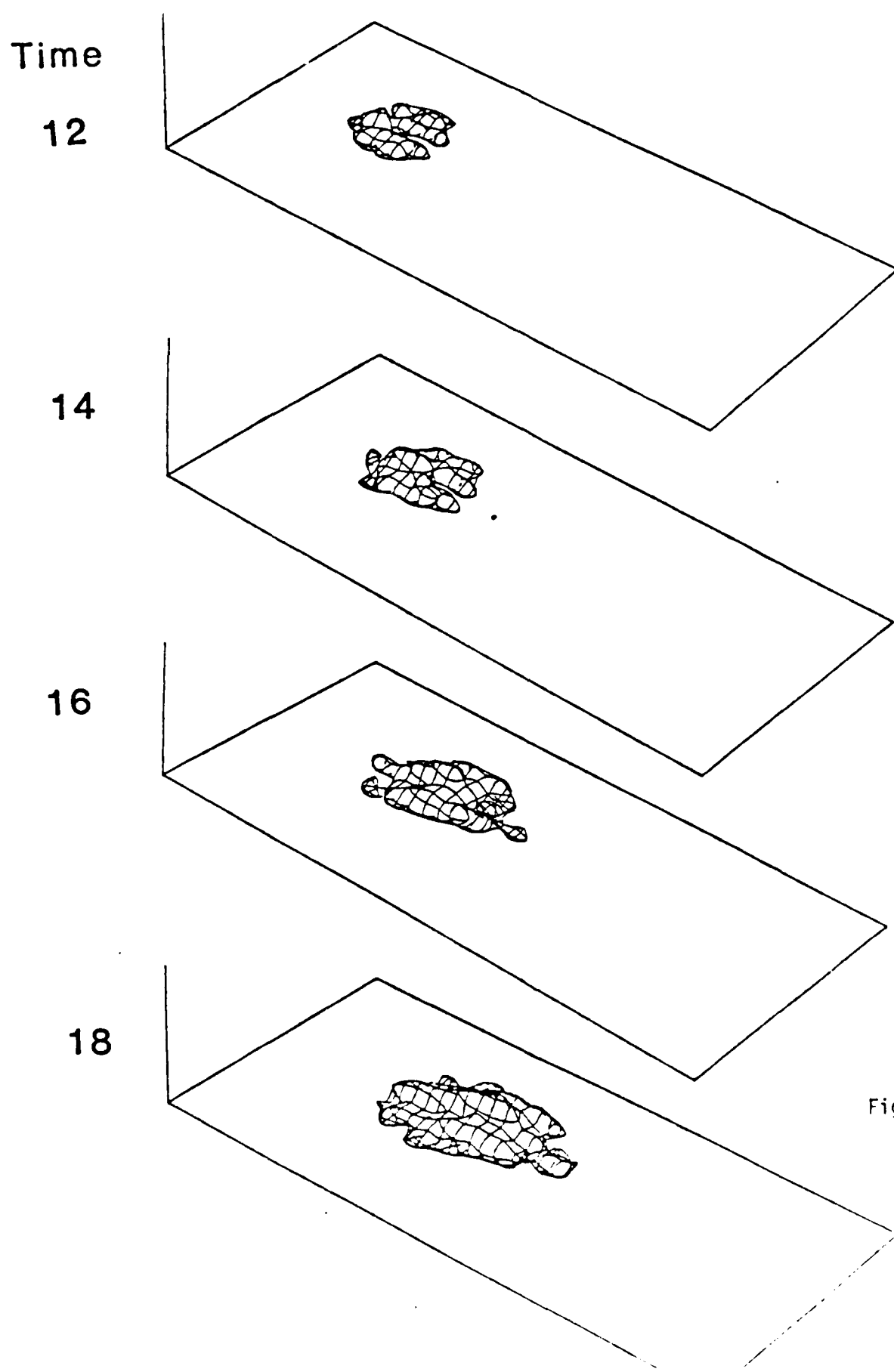


Figure 9

$t = 30$

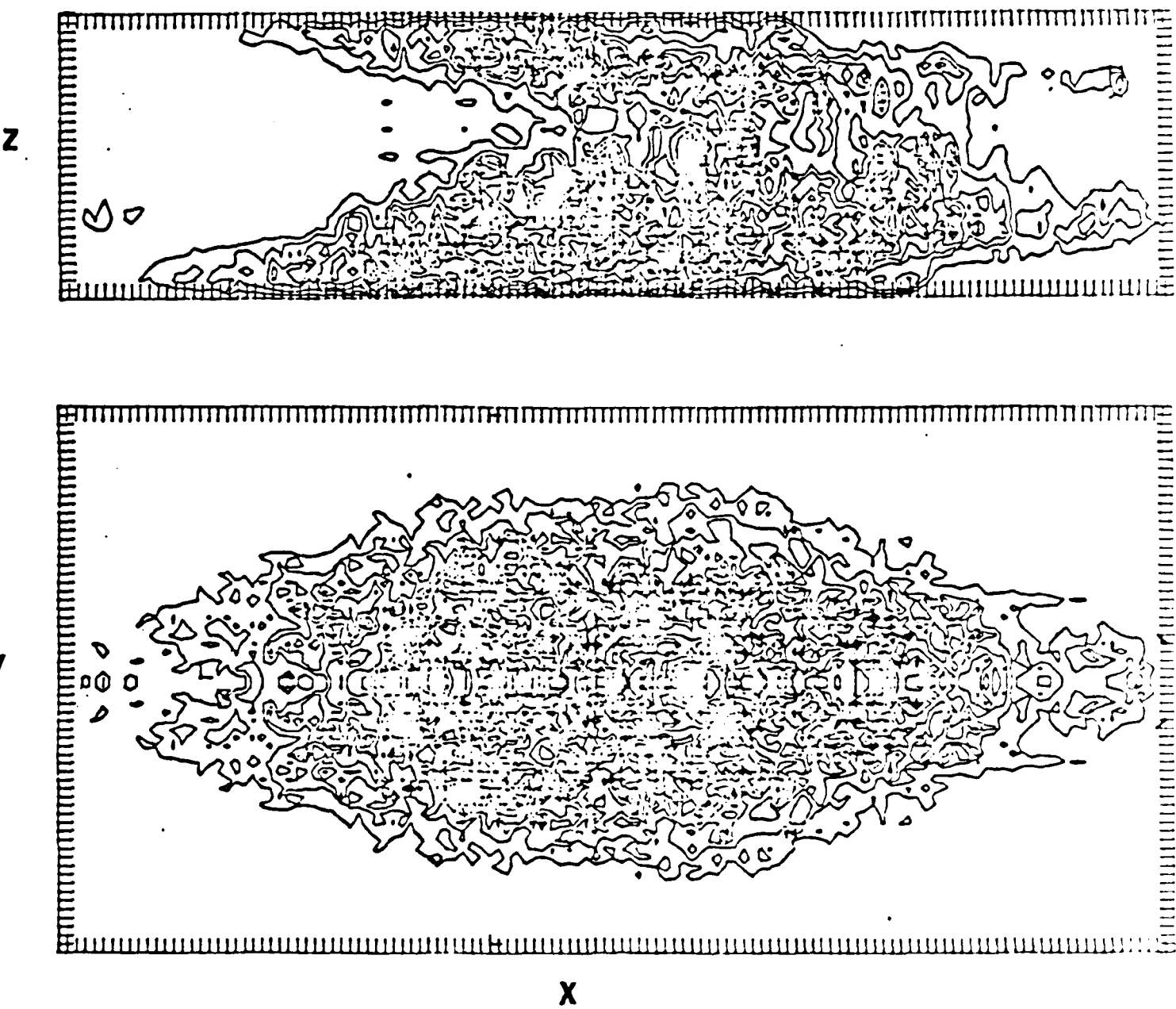


Figure 10

MEAN VELOCITY PROFILES
AT CENTER AND EDGE OF SPOT

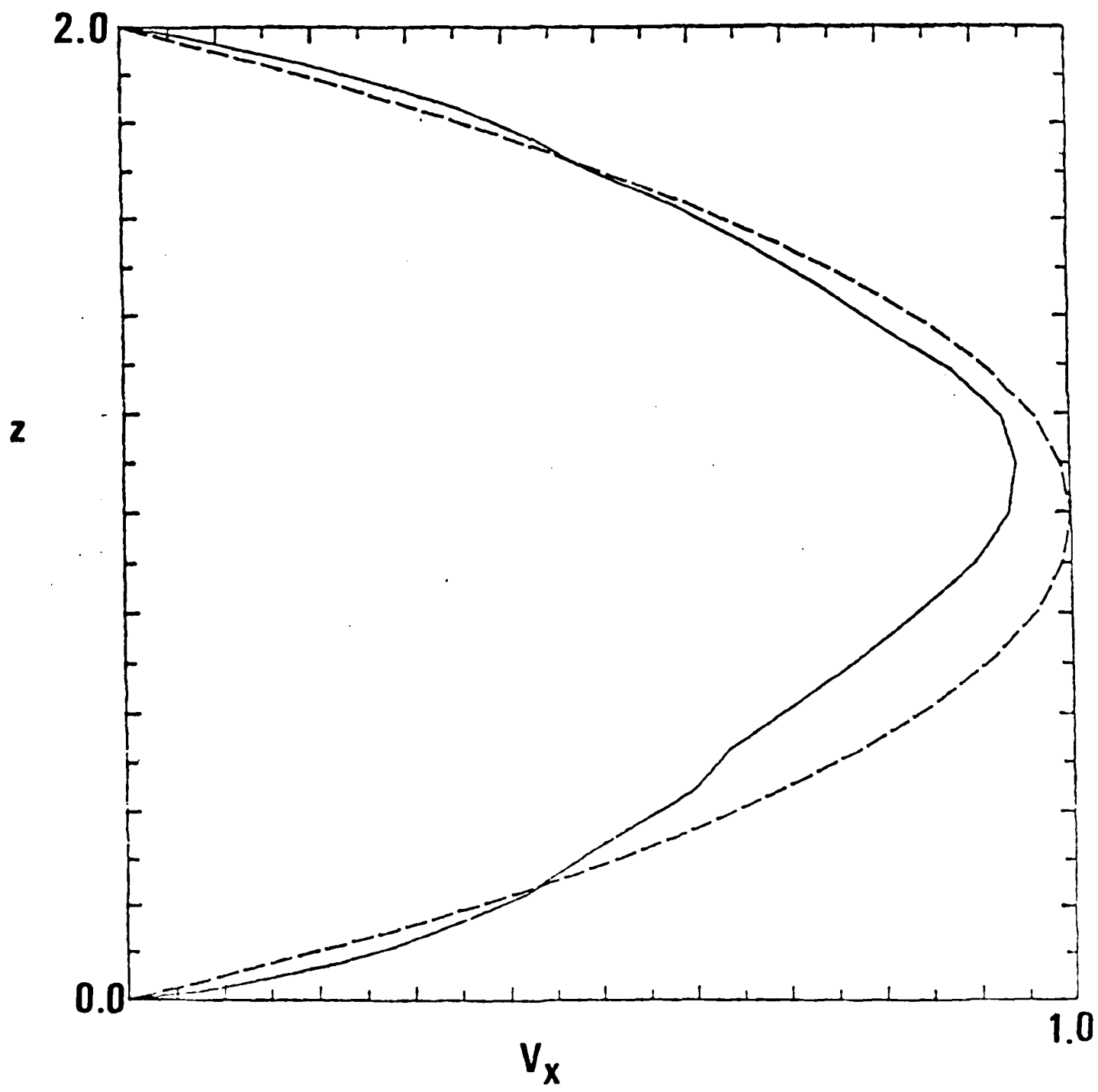


Figure 11

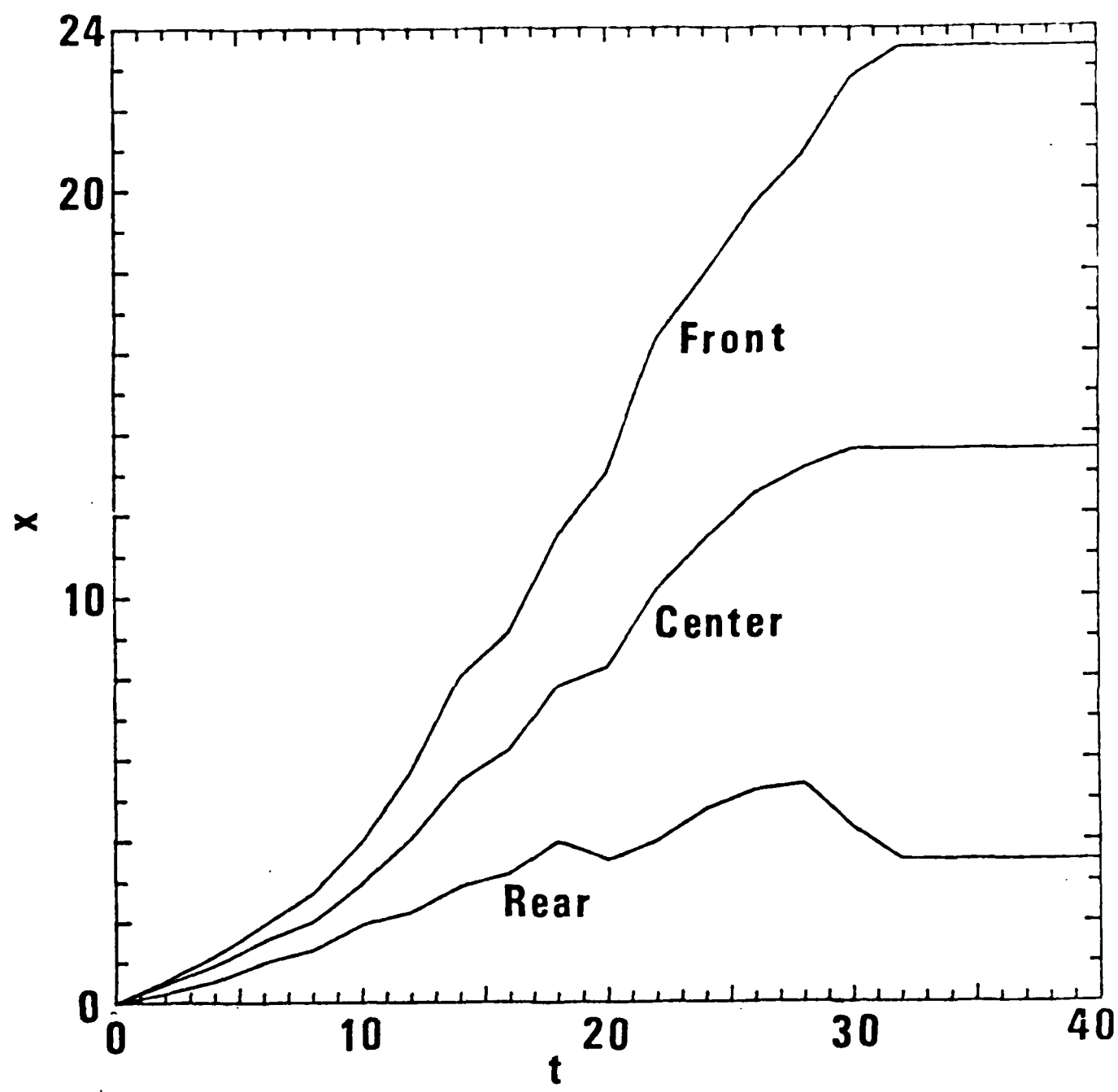
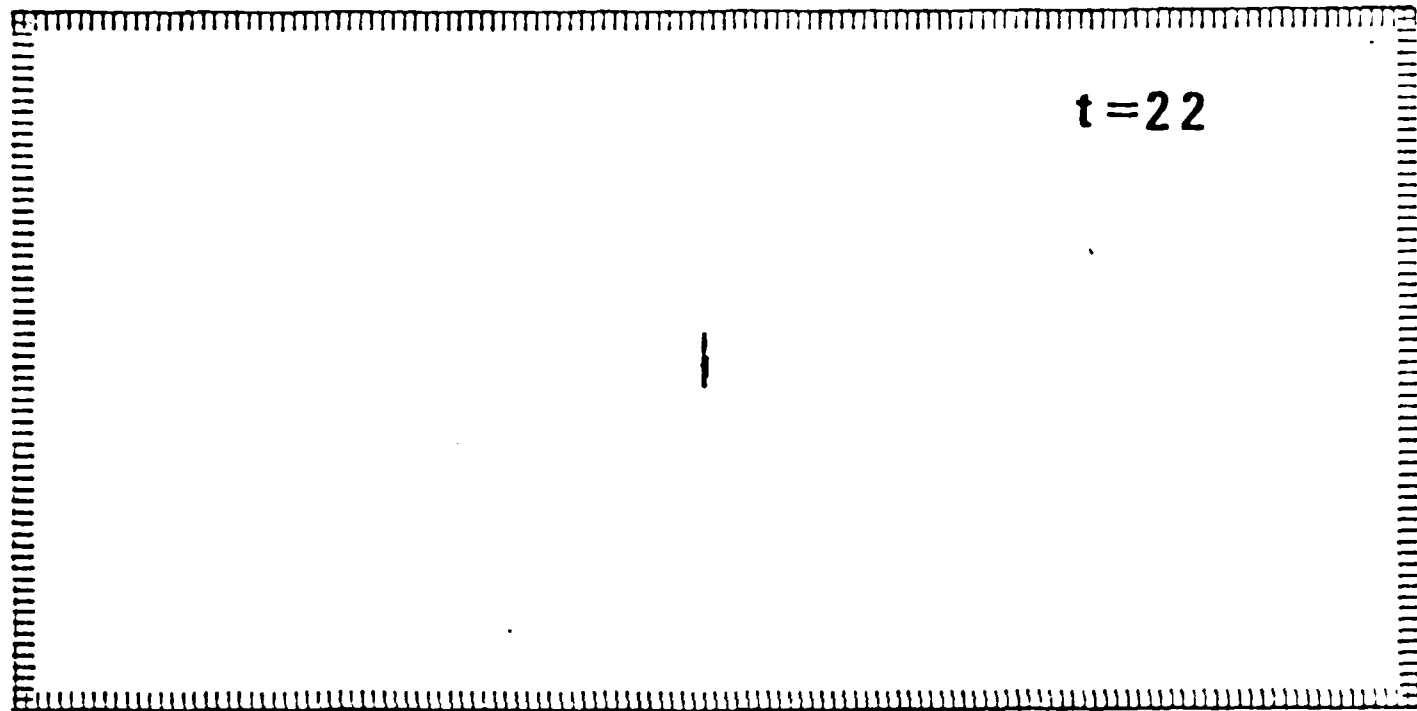
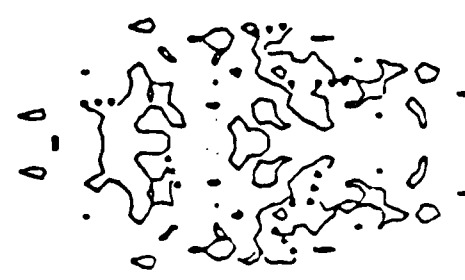


Figure 12

$t = 22$



$t = 24$



x

Figure 13

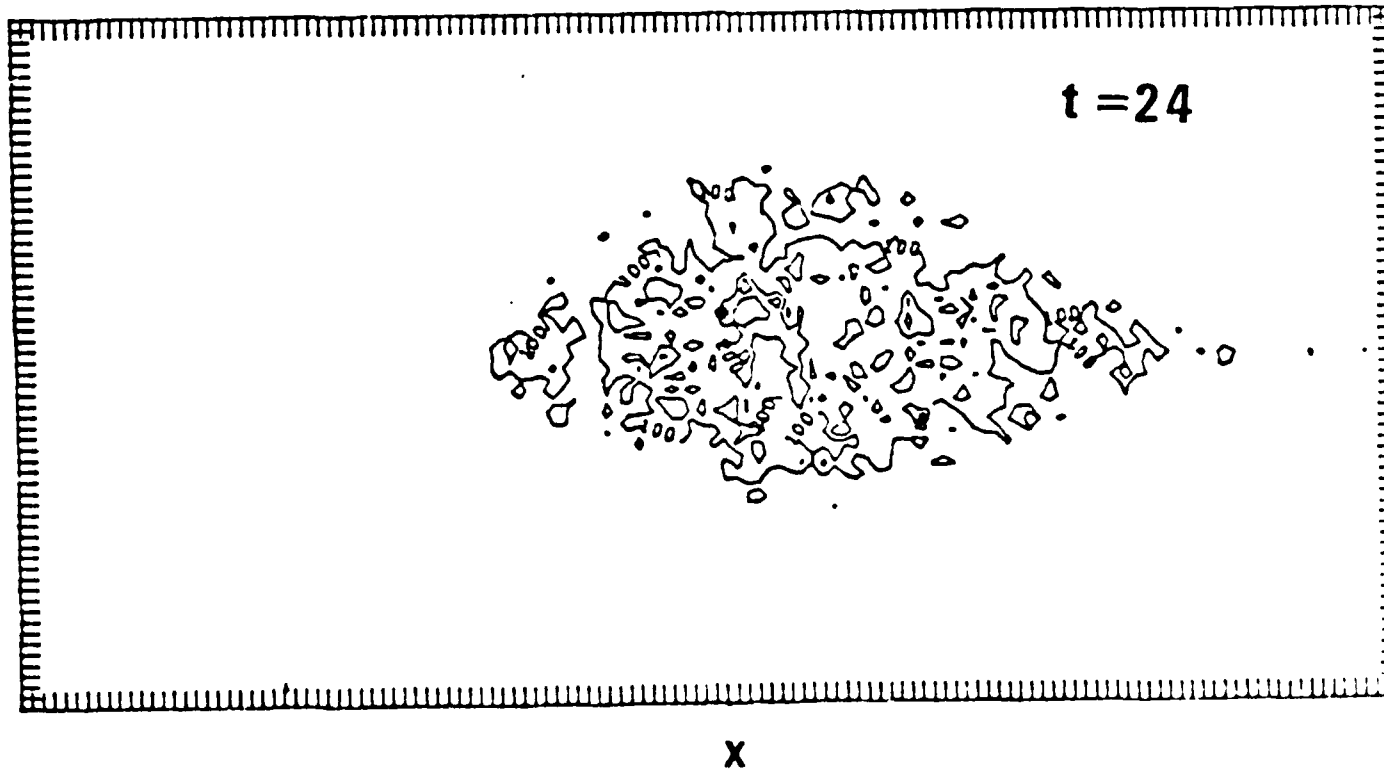
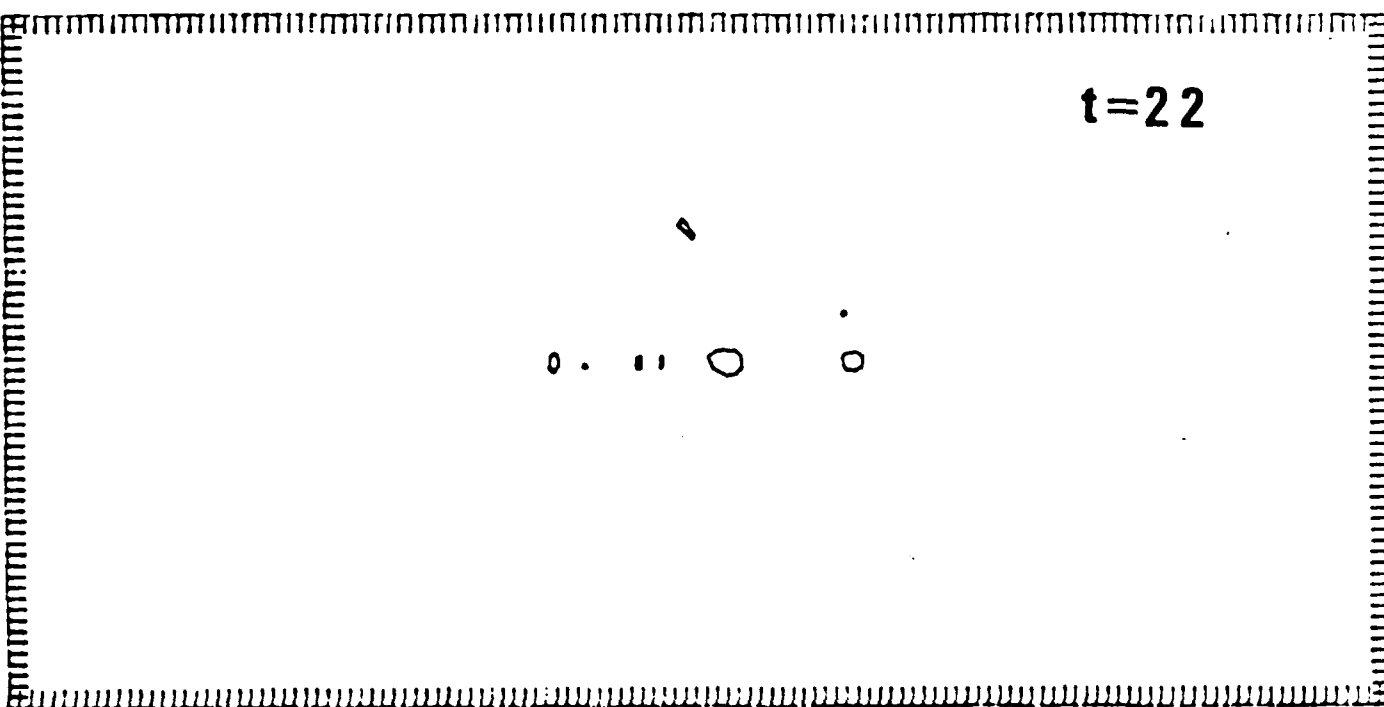


Figure 14

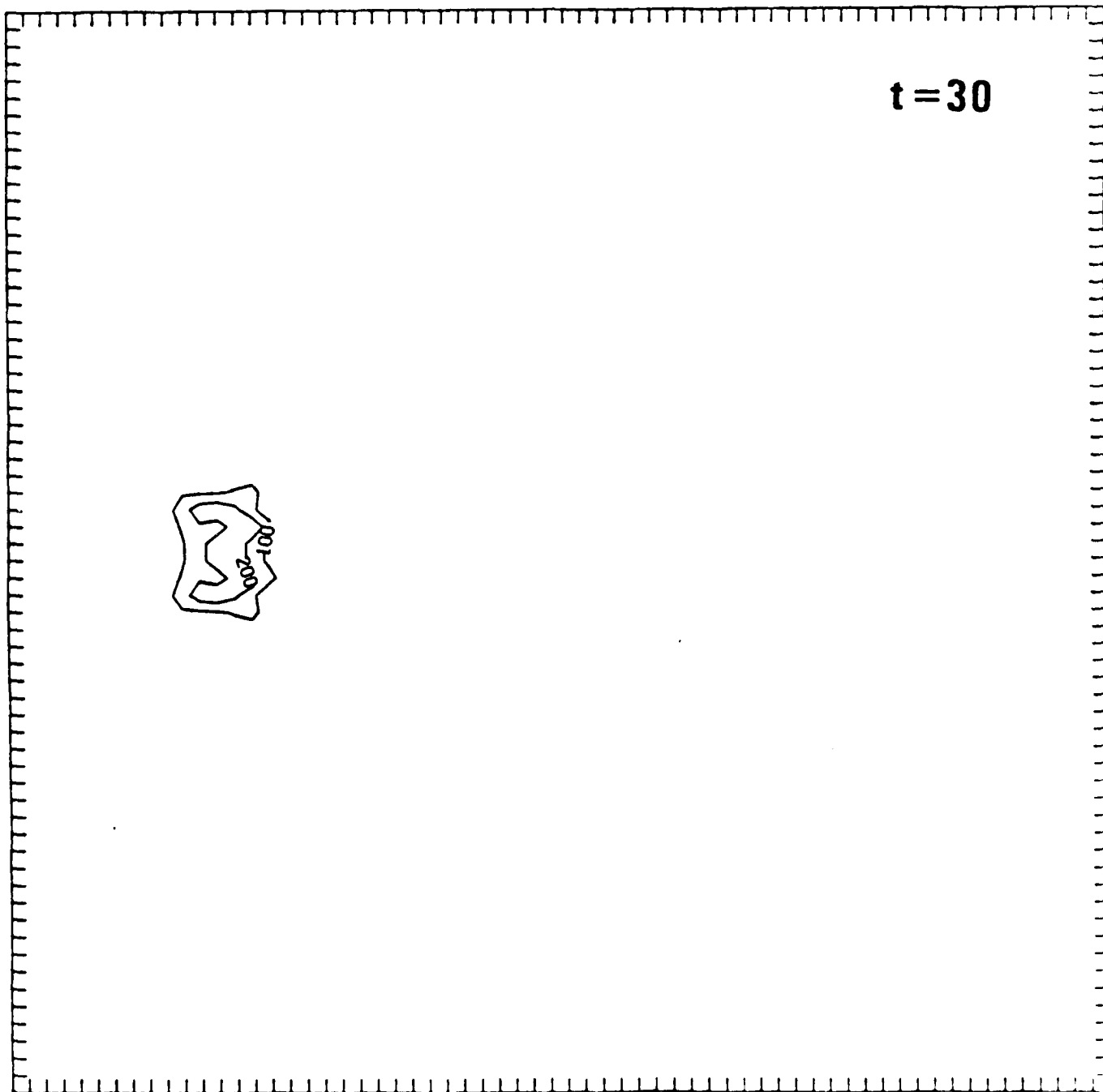


Figure 15a

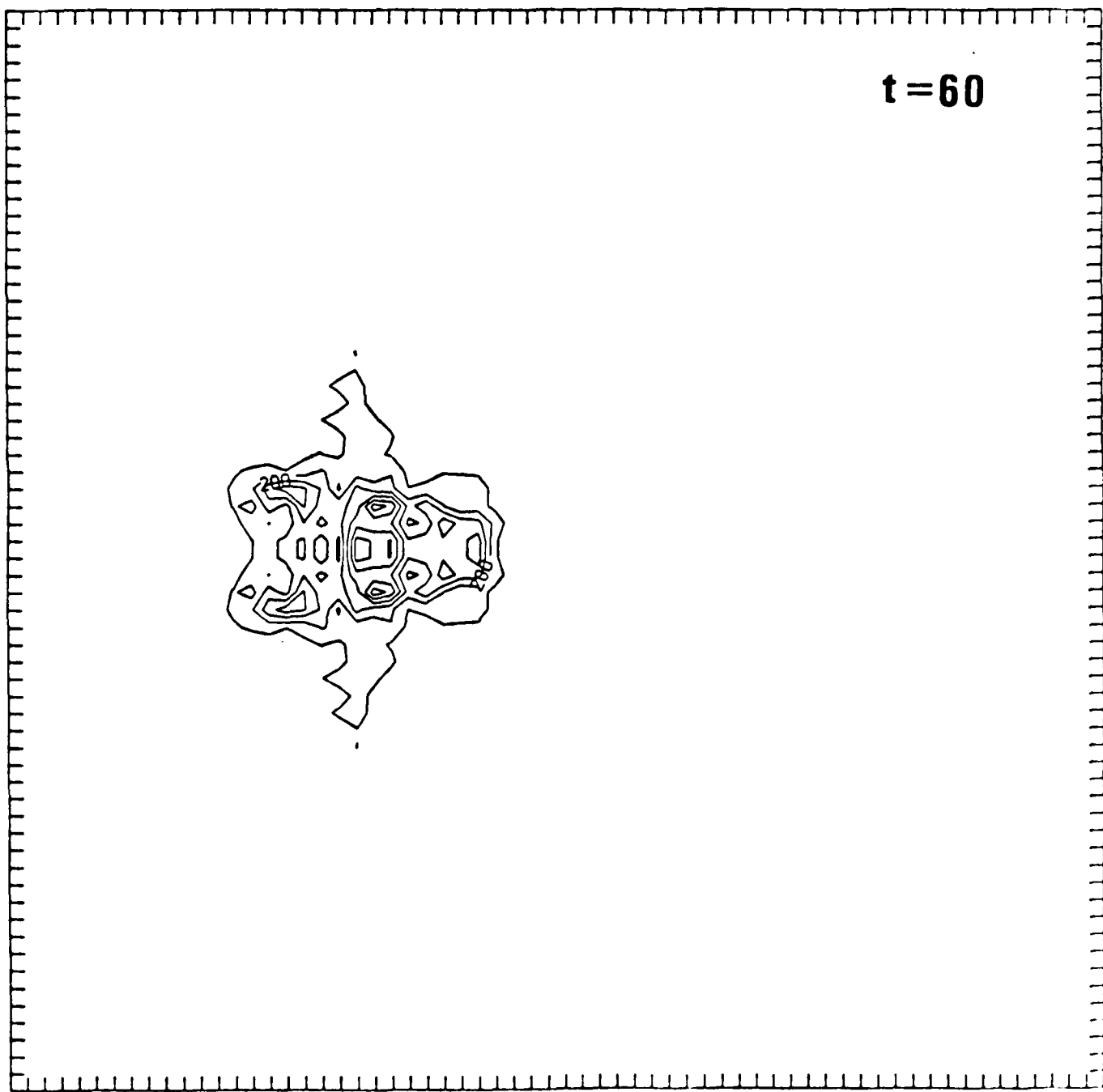
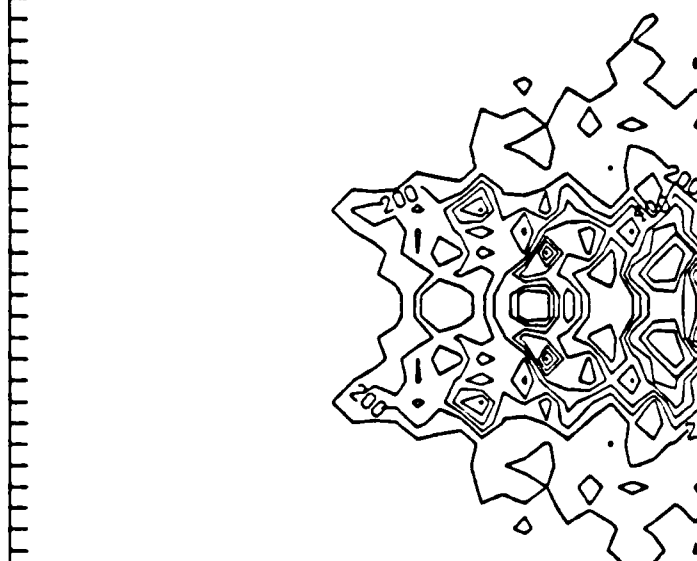


Figure 15b

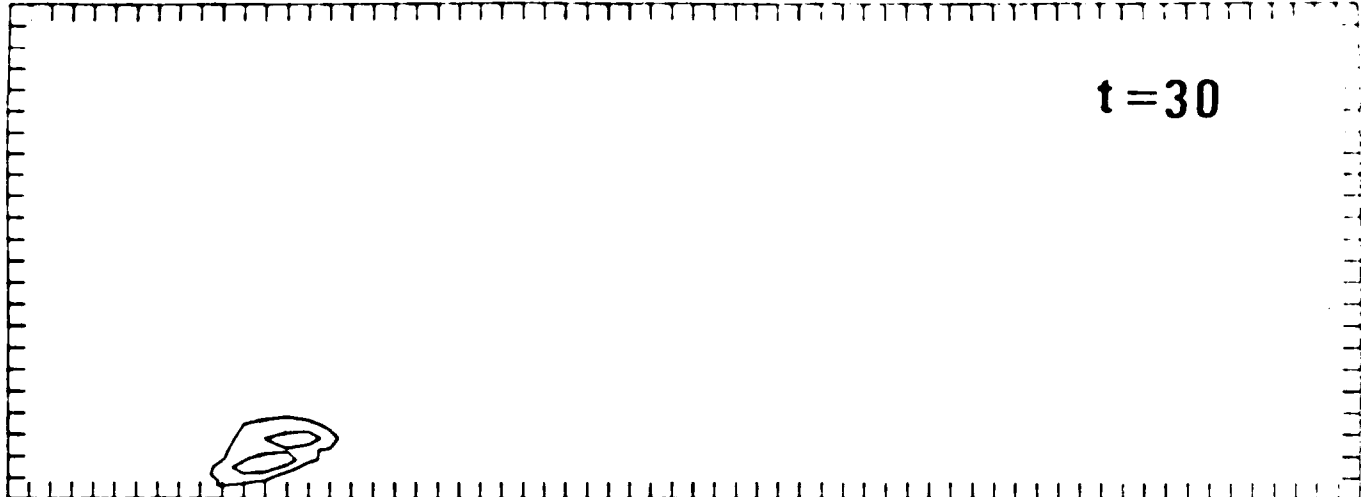
$t = 90$



y

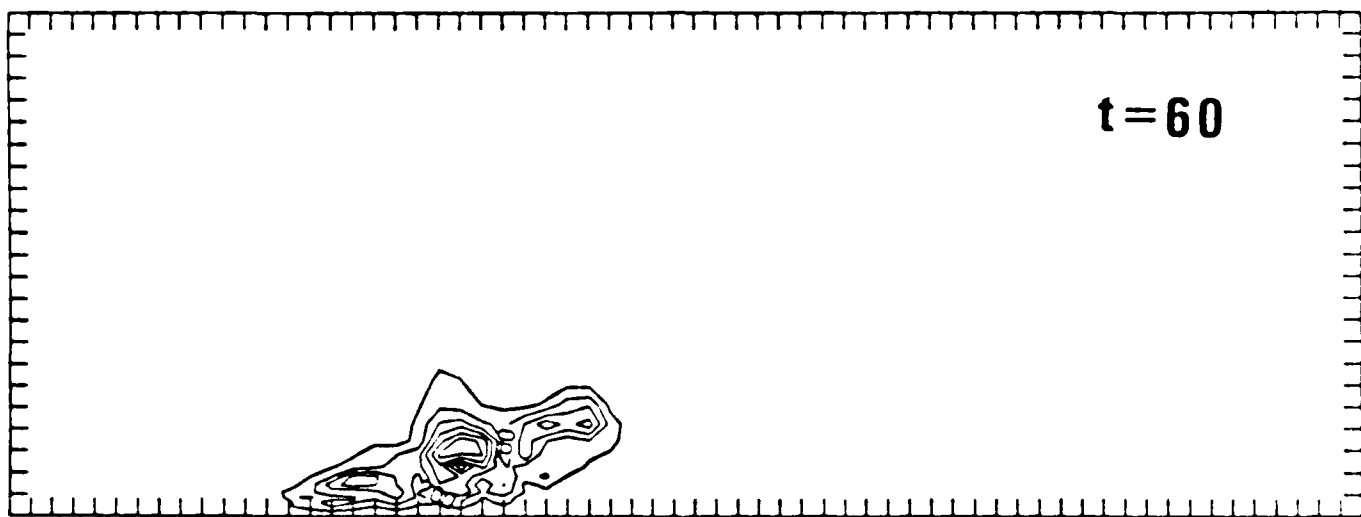
x

Figure 15c



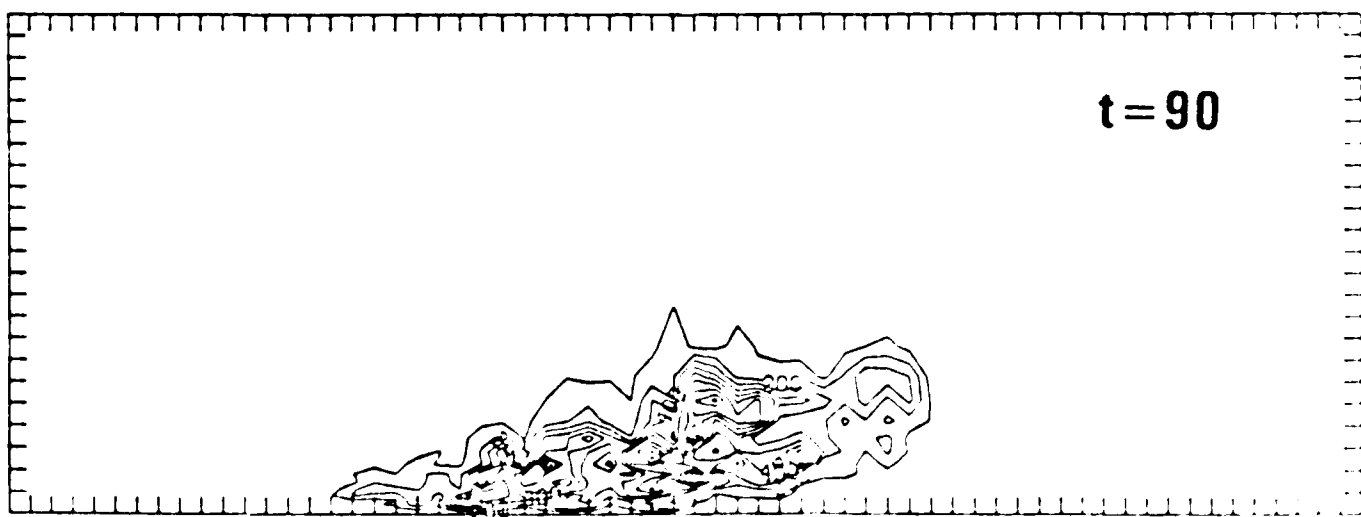
$t = 30$

(a)



$t = 60$

(b)



$t = 90$

(c)

Figure 16

$t = 30$

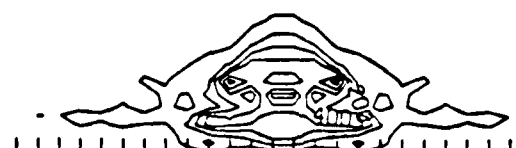
z



(a)

$t = 60$

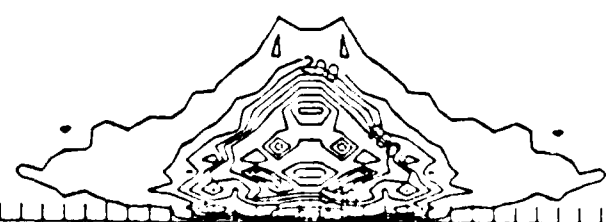
z



(b)

$t = 90$

z



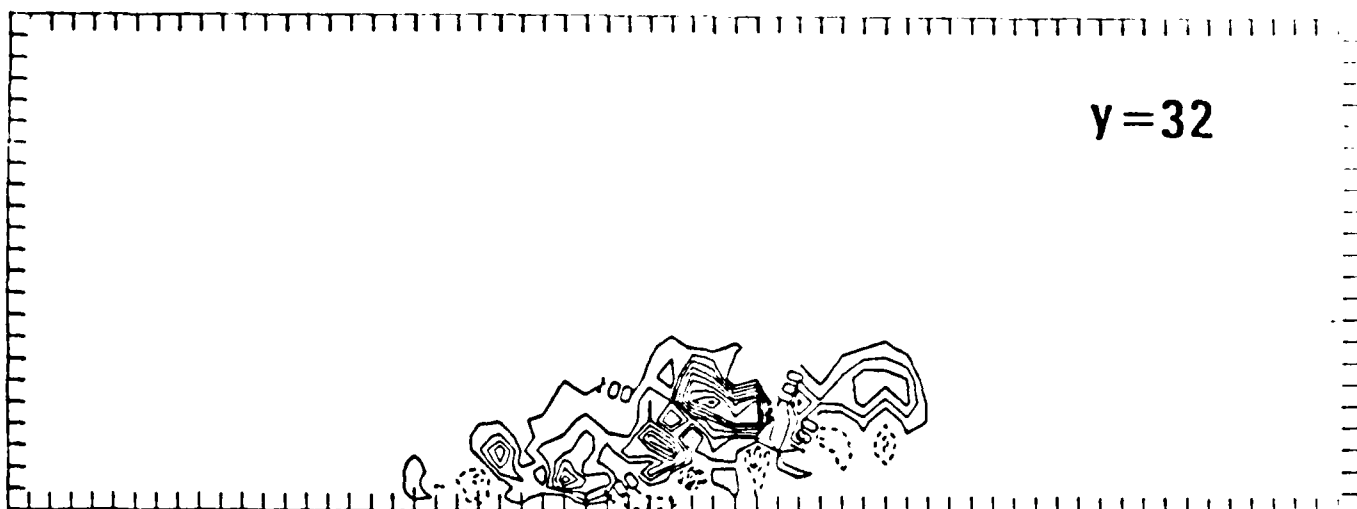
y

(c)

Figure 17

$\gamma = 32$

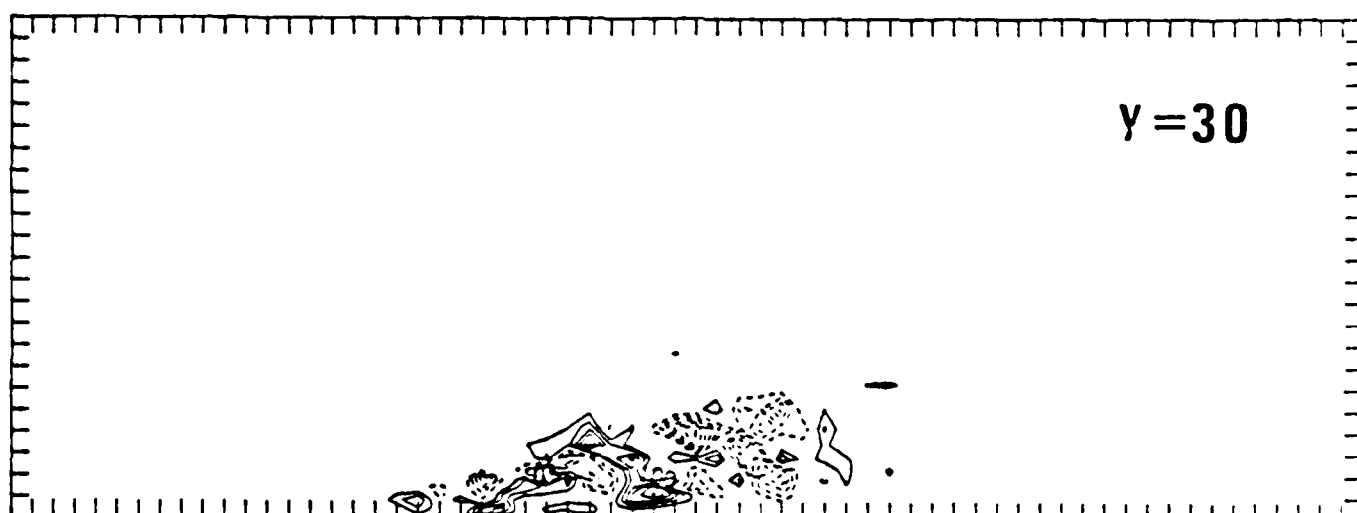
Z



(a)

$\gamma = 30$

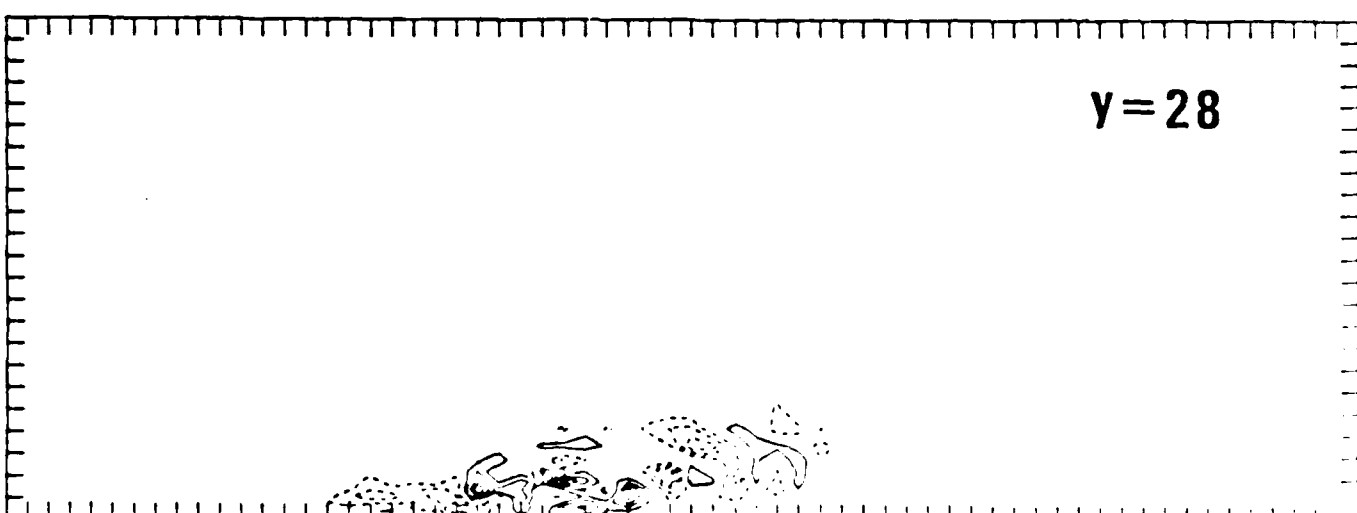
Z



(b)

$\gamma = 28$

Z



(c)

Figure 15

END

11 - 87

DTIC